Respiratory Airway Secretory Cells act as Immune Sentinels in Human Distal Airways

Jiaqi Sun[1,2], Hui Sun[1,2], Shisheng Jiang[1,2], Xiaoxiao Xie[1,2], Dong Wang[5], Hongjie Yao[1], Weijie Guan[1,3], Jincun Zhao[1,3]*, Wei Kevin Zhang[1,4]*, Tao Xu[1,2]*, Huisheng Liu[1,2]*

1 Guangzhou National Laboratory, Guangzhou, Guangdong, China

2 School of Biomedical Engineering, Guangzhou Medical University, Guangzhou, Guangdong, China

3 State Key Laboratory of Respiratory Disease, National Clinical Research Center for Respiratory Disease, Guangzhou Institute of Respiratory Health, The First Affiliated Hospital of Guangzhou Medical University, Guangzhou, Guangdong, China

4 School of Pharmaceutical Sciences, Guangzhou Medical University, Guangzhou, Guangdong, China

5 GMU-GIBH Joint School of Life Sciences, Guangzhou Medical University, Guangzhou, Guangdong, China

* Corresponding author. Email: liu_huisheng@gzlab.ac.cn; xu_tao@gzlab.ac.cn; zhaojincun@gird.cn; zhang_wei@gzlab.ac.cn

Abstract

Pulmonary immunity is essential for maintaining lung function by protecting against infection and injury[1,2]. As the distal respiratory airways (also termed terminal and respiratory bronchioles) are structures unique to humans and other

large mammals, the cellular mediators of immunoregulation in this region remain elusive. Here, using human pluripotent stem cell-derived lung organoids and clinical specimens, we reveal previously unrecognized innate immune defense in human distal airways mediated by respiratory airway secretory (RAS) cells. Lineage tracing identified RAS cells as descendants of SOX9^{bright}NKX2-1^{bright} progenitors. Single-cell transcriptomics elucidated that RAS cells exhibited a distinct immune-competent phenotype, characterized by enrichment of genes associated with viral host entry and pattern recognition receptor signaling. Functionally, RAS cells exhibited enhanced antiviral activity against respiratory syncytial virus by upregulating interferon-stimulated genes. Furthermore, upon stimulation with bacterial flagellin or *Pseudomonas aeruginosa* (PAO1), RAS cells initiated robust immune responses through TLR5 activation, resulting in CXCL8 release to recruit and activate neutrophils[3], which was markedly suppressed by a selective TLR5 inhibitor. Notably, RAS cells from chronic obstructive pulmonary disease patients with PAO1 infection showed significant secretion of chemokines, including CXCL8 and CXCL10, directly linking these cells to disease-associated inflammation. Collectively, our findings establish RAS cells as critical immune sentinels in the human distal respiratory airways, filling a gap in understanding human distal lung immunity and its role in maintaining lung function and chronic lung diseases.

45 **Main**

46 The human respiratory tract orchestrates air exchange while defending against
47 pathogens through specialized epithelial cells. Unlike mice, humans possess respiratory
48 airways or terminal and respiratory bronchioles (RA or TRBs)—transitional structures
49 within the distal airways that are critical for efficient respiration in large mammals[4,5].
50 Many respiratory diseases, such as chronic obstructive pulmonary disease (COPD)[6,7],
51 pulmonary fibrosis[8,9], and viral infections[10,11], disrupt these bronchioles through
52 inflammation and remodeling, which impairs respiratory function by increasing airflow
53 resistance and reducing clearance mechanisms. Despite their clinical importance, the
54 immunological mechanisms protecting these structures remain poorly understood,
55 partly due to the lack of models recapitulating human-specific biology.

56 Recent breakthroughs have identified unique SCGB3A2-expressing secretory cell
57 populations within the human distal airways[12]. Respiratory airway secretory (RAS)
58 cells serve as progenitors for alveolar type 2 (AT2) cells[13]. TRB-secretory cells (TRB-
59 SCs) and alveolar type 1 (AT1) cells differentiate from AT2 cells via an intermediate
60 AT0 state[14]. However, the immunological role of these secretory cells remains
61 unexplored.

62 Here, we integrate human pluripotent stem cell (hPSC)-derived lung organoids—
63 a model recapitulating human-specific distal airway development—with single-cell
64 transcriptomics and clinical specimens to establish RAS cells as innate immune
65 sentinels. We demonstrate that RAS cells mount robust antiviral defenses against
66 respiratory syncytial virus (RSV) and exhibit high TLR5 expression, which drives

robust immune responses to flagellated bacteria. Strikingly, RAS cells from COPD patients with PAO1 infection amplify chemokine secretion, mirroring disease-associated immune dysregulation. Together, our findings reveal a novel epithelial innate immune defense functions mediated by RAS cells within the human distal respiratory airways.

Robust Generation of Distal Lung Organoids

Human lung development relies on spatially distinct progenitor populations: SOX2^{bright}NKX2-1^{dim} proximal lung progenitor cells (p-LPC) drive airway differentiation, while SOX9^{bright}NKX2-1^{bright} distal lung progenitor cells (d-LPC) are critical for branching morphogenesis and alveologenesis (Fig. 1a)[15-19]. To generate SOX9^{bright}NKX2-1^{bright} distal lung progenitors from hPSCs, we utilized and modified previously reported protocols for definitive endoderm (DE) and 3D anterior foregut endoderm (AFE) spheroid induction (Extended Data Fig. 1a)[20]. Inspired by successful colon organoid systems that dissociate hindgut endoderm into Matrigel[21], we dissociated AFE spheroids into single cells and embedded them in 3D Matrigel droplets (Fig. 1b). This dissociation step dramatically increased organoid yield (>4-fold) and uniformity (Extended Data Fig. 1b–e).

Transcript analysis of lung progenitor markers (*SOX2*, *SOX9*, *NKX2-1*) revealed that dissociation significantly upregulated *NKX2-1* expression (10- to 100-fold), with minimal changes in *SOX9* and *SOX2* levels (Fig. 1d, Extended Data Fig. 1i). Triple immunostaining confirmed enrichment of SOX9^{bright}NKX2-1^{bright} cells in dissociation-

89 treated cultures, whereas SOX2^{bright}NKX2-1^{dim} populations dominated untreated
90 conditions (Fig. 1c). Flow cytometry further validated elevated NKX2-1 protein levels
91 in dissociated organoids (Extended Data Fig. 1f–h). Aligning with embryonic lung gene
92 expression patterns[15], we designated organoids from untreated conditions as proximal
93 lung organoids (p-LOs) and those from dissociated cultures as distal lung organoids (d-
94 LOs). The protocol consistently generated d-LOs across multiple hPSC lines,
95 underscoring its robustness and broad applicability (Extended Data Fig. 1i).
96
97 **Characterization of d-LOs**
98 To validate the distal identity of d-LOs, we performed single-cell RNA sequencing
99 (scRNA-seq) on 10,815 cells from p-LOs and d-LOs at day 8. Our analysis identified
100 three cellular compartments: epithelial, mesenchymal, and neural cells (Extended Data
101 Fig. 2a, b). We then extracted and reclustered the epithelial cells for a more detailed
102 investigation (Fig. 1e, f and Extended Data Fig. 2c). Six cell clusters were annotated
103 based on their distinct molecular features: d-LPC, p-LPC, cycling, neuroendocrine,
104 hindgut, and an unknown population. Notably, d-LPC cluster was abundantly generated
105 in d-LOs (43.01% in d-LOs and 0.71% in p-LOs; Fig. 1g), while p-LPC was enriched
106 in p-LOs (12.33% in d-LOs and 37.29% in p-LOs; Fig. 1g), corroborating gene/protein
107 data.
108 Benchmarking against human fetal lung datasets[15] further confirmed proximal-
109 distal divergence (Fig. 1h and Extended Data Fig. 2f): p-LPC in p-LOs expressed
110 proximal markers (e.g., *SOX2*, *DMD*, *SEMA3C*, *KREMEN1*, and *MIR99AHG*), while

111 d-LPC in d-LOs upregulated distal regulators (e.g., *SOX9*, *ETV1*, *SOX6*, and *GATA*).
112 Notably, ETV1 and SOX6 are human development-specific transcription factors
113 involved in distal lung patterning[15]. Gene Ontology analysis of differentially expressed
114 genes (DEGs) within the p-LPC and d-LPC clusters reinforced their proximal and distal
115 identities (Extended Data Fig. 2d-e). Specifically, p-LPC genes are involved in cilium
116 organization and assembly, while d-LPCs are enriched for genes associated with
117 epithelial tube morphogenesis and branching morphogenesis, with high gene-
118 expression levels of *NKX2-1*, *SOX9*, *WNT7B* and low *SFTPC*, mirroring 7–8 post-
119 conception weeks (pcw) fetal lung bud tips[19]. Collectively, these data strongly suggest
120 that the d-LPC population in d-LO closely recapitulates the transcriptional profile and
121 functional characteristics of early human lung bud tip cells.
122
123 **Differentiation potential of d-LOs**
124 While existing lung organoids model proximal airways or alveoli[22], respiratory
125 bronchioles—a human-specific transitional zone—remain scarce. To assess the fate
126 potential of d-LOs in our system, we cultured p-LOs and d-Los either in airway
127 (DCIK)[23] or in alveolar (DCIK+CSB) media[24] (Extended Data Fig. 3a). We found that
128 p-LO-derived airway organoids (p-AWO) expressed higher levels of proximal airway
129 genes like *TP63* and *MUC5AC*, while d-LO-derived airway organoids (d-AWO)
130 showed elevated expression of distal airway lineage genes, including *SCGB3A2* (a
131 distal club cell marker), and alveolar lineage markers (*SFTPB*, *AGER*, *PDPN*, and
132 *LAMP3*) (Extended Data Fig. 3b). For alveolar induction, only d-LOs cultured in

133 DCIK+CSB media (d-ALO) exhibited robust alveolar differentiation, marked by high
134 levels of *SFTPB*, *SFTPC*, *NKX2-1*, and *LAMP3*, consistent with the requirement of
135 NKX2-1 for distal lung development. Notably, *SCGB3A2* was modestly expressed in
136 d-ALO. Immunostaining further confirmed that d-LOs readily differentiate into distal
137 airway and alveolar organoids, with abundant SCGB3A2 and SFTPB co-expressing
138 cells, which are absent in p-AWO (Extended Data Fig. 3c). Collectively, these findings
139 suggest that p-LOs predominantly generates proximal airway organoids, while d-LOs
140 uniquely models human distal airway and alveoli (Extended Data Fig. 3d).

141 Additionally, d-LO-derived organoids demonstrated functional properties,
142 including CFTR-dependent forskolin swelling (Extended Data Fig. 4a-b) and BODIPY-
143 labeled phosphatidylcholine uptake and secretion (Extended Data Fig. 4e-f). Beating
144 cilia were visible (Supplementary Video 1) in apical-out d-AWO released from
145 Matrigel[25] (Extended Data Fig. 4c). Transmission electron microscopy (TEM) analysis
146 of d-ALOs revealed lamellar body-like organelles (Extended Data Fig. 4d). In summary,
147 these results indicate that d-LOs can efficiently generate distal airway and alveolar
148 organoids with functional and structural features characteristic of mature lung tissue.

149

150 **RAS cells in d-LO-derived organoids**

151 To further investigate the unique cell type in d-LO-derived organoids, we performed
152 scRNA-seq on p-AWO (D35), d-AWO (D35 and D90) and d-ALO (D35 and D90)
153 (Extended Data Fig. 3a, 5a-b). Cell populations were annotated using differentially
154 expressed genes and correlated with established cell signatures from prior studies[26]

155 (Extended Data Fig. 5c-d). Both p-AWO and d-AWO showed abundant basal and
156 proximal secretory cells, alongside smaller populations of club cells, ciliated cells, and
157 pulmonary neuroendocrine cells (PNECs). AT2 cells were abundant in d-ALO (D90)
158 (Fig. 2a-c). Notably, we identified a distinct population of SCGB3A2^{+}SFTPB^{+}SFTPC^{-}
159 cells, which we termed respiratory airway secretory cells (RAS cells), in d-LO-derived
160 organoids, confirming their resemblance to human distal respiratory airways. This
161 unique cluster, positioned between the d-LPC, proximal secretory, PNEC, and AT2
162 clusters on the UMAP embedding (Fig. 2a and Extended Data Fig. 5c), exhibited a
163 specific gene expression profile, including markers such as *MUC1*, *CFTR*, *CEACAM6*,
164 *SLC4A4*, and *STEAP4* (Extended Data Fig. 5e), with MUC1 and CEACAM6 serving
165 as cell surface markers for these specialized secretory cells[13,27].

166 Additionally, when transplanted under the kidney capsule of immunodeficient
167 NSG mice, d-ALOs formed growths containing both tubular and sac structures after 4
168 weeks (Extended Data Fig. 4g-i). The tubular structures were lined by NKX2-
169 1^{+}SCGB3A2^{+} epithelium, which also expressed SFTPB (Fig. 2d), mirroring the distal
170 characteristics of human fetal lung tissue at 19-20 pcw[14]. Collectively, these findings
171 underscore the unique differentiation potential and functional relevance of d-LO-
172 derived organoids in modeling human respiratory airways.

173

174 **A d-LPC–RAS cell relationship**

175 Research shows that SCGB3A2-expressing cells emerge as early as 5 pcw in fetal
176 lungs[28]. To explore the developmental trajectory of RAS cells, we integrated scRNA-

177 seq data from d-LOs and d-LO-derived organoids (Extended Data Fig. 6a-c). Trajectory
178 inference analysis using Monocle3 revealed a strong cell trajectory originating from the
179 d-LPC cluster into RAS cell cluster (Fig. 2e-g). The gene expression changes along the
180 d-LPC–RAS cell trajectory highlighted several genes known to be involved in secretory
181 and alveolar differentiation, including *SCGB3A2*, *SFTPB* and *HOPX* (Extended Data
182 Fig. 5f-g). Additionally, transcription factors like *AHR*, *GRHL1*, and *SOX2*, identified
183 through pseudotime analysis, showed strong correlations with primary distal airway
184 secretory cells[14].

185 Further analysis of the integrated dataset demonstrated pseudotemporal
186 relationships between RAS cells and basal, PNEC, and AT2 cells (Fig. 2e-f, Extended
187 Data Fig. 6d-g), indicating that RAS cells may function as progenitors for human distal
188 lung development and regeneration. Trajectory inference also indicated a
189 developmental link between p-LPC and ciliated cells (Extended Data Fig. 6h). Together,
190 these in silico predictions suggest that d-LPC acts as a putative progenitor for the RAS
191 cell lineage, which can subsequently give rise to basal, PNEC, and AT2 cells.

192

193 **RAS cells exhibit immune functions**

194 Transcriptomic profiling of the differentiation trajectory from d-LPC to RAS cell
195 identified dynamic expression changes in genes associated with immune regulation,
196 including *RUNX1*, *CD55*, *MUC1*, *SCGB3A2*, *TXNIP*, *CEBPD*, *S100A6*, and *S100A10*.
197 Differential gene expression (DGE) analysis between d-LPCs and RAS cells further
198 demonstrated elevated expression of immune-related transcripts in RAS cells, including

199 mucins (*MUC1*, *MUC4*), surfactant proteins (*SFTPB*, *SFTPD*), cytokines (*CXCL8*,
200 *CCL20*), and cell adhesion molecules (*ICAM5*, *ITGB6*) (Fig. 2h). Gene set enrichment
201 analysis (GSEA) of the DEGs revealed significant enrichment of immune-associated
202 pathways, such as antibacterial responses, regulation of viral entry into host cells, and
203 positive regulation of pattern recognition receptor (PRR) signaling. These findings
204 align with recent reports describing the immunomodulatory functions of TRB-SCs from
205 the human distal airways[14]. Together, these results establish a broad spectrum of
206 immune-related transcriptional activity in RAS cells, emphasizing their pivotal role in
207 respiratory immune defense.
208

209 **RAS cells show antiviral responses upon RSV infection**

210 Considering the clinical relevance of RSV infections in distal airways in vulnerable
211 individuals—a primary cause of bronchiolitis and pneumonia[29], we thus evaluated RSV
212 susceptibility using our distal organoid model.

213 RSV exhibited robust replication kinetics at a low multiplicity of infection (MOI
214 = 0.1), as quantified in both supernatant and cell lysates (Fig. 3a). Morphological
215 analysis of infected d-ALOs revealed significant epithelial malformations, including
216 cytoskeletal reorganization and syncytia formation, mirroring clinical hallmarks of
217 RSV infection[30] (Fig. 3b). Notably, SCGB3A2-positive cells were extensively targeted
218 by RSV, as confirmed by co-staining for SCGB3A2 and RSV-F. Furthermore, RSV-
219 infected organoids showed significant upregulation of pro-inflammatory cytokines
220 (*CXCL8*, *CXCL10*, *TNF-α*, *IL-6*) relative to mock-infected controls (Extended Data Fig.

221 7a). To further explore the cellular response to infection, we performed scRNA-seq on
222 mock- and RSV-infected organoids. The scRNA-seq data revealed a high infection rate,
223 with viral transcripts detected in nearly all cells (Fig. 3c). However, viral gene
224 expression was unevenly distributed, with most cells showing low levels of viral
225 transcripts and a smaller subset (two distinct clusters) exhibiting significantly higher
226 levels—one within RAS cells and the other among non-epithelial cells.

227 To identify RAS cell-specific molecular changes induced by RSV infection,
228 differential gene expression analysis was performed between highly infected RAS cells
229 (RAS cell^{high}) and other infected clusters, as well as between low-infected RAS cells
230 (RAS cell^{low}) and their mock-treated counterparts. Gene Ontology analysis of DEGs
231 revealed consistent upregulation of terms such as "response to virus" and "viral life
232 cycle" across all analyzed clusters (Extended Data Fig. 7b-e). Significant overlap was
233 observed among DEGs from multiple comparisons, with strong enrichment for
234 immune-related functions, including "defense response to virus", "antiviral innate
235 immune response", "NF-kappa B signaling pathway", and "antigen presentation" (Fig.
236 3d, f). Furthermore, we observed broad induction of interferon-stimulated genes (ISGs)
237 (Fig. 3e), including viral entry inhibitors (*MX1*, *MX2*, *IFITM1*, *TRIM22*) and the egress
238 suppressor *RSAD2*, indicative of a potent interferon-mediated antiviral state in RAS
239 cells. These findings collectively establish that RAS cells mount a markedly enhanced,
240 cell type-specific antiviral response upon viral challenge.

241

242 **RAS cells display inflammatory responses via activation of TLR5**

243 GSEA revealed significant enrichment of Toll-like receptor (TLR) signaling pathway
244 genes in RAS cells (Fig. 2i), a pathway central to respiratory tract host defense[31].
245 Notably, TLR5—a flagellin sensor—was specifically upregulated in RAS cells (Fig.
246 4a-b), aligning with scRNA-seq data from early human fetal lung tissue identifying a
247 $SCGB3A2^{+}SFTPB^{+}CFTR^{+}$ subpopulation co-expressing TLR5[32]. Immunostaining
248 further validated robust TLR5 protein expression in RAS cells within organoids (Fig.
249 4c, e).

250 To assess the functional role of TLR5 activation in RAS cells during defense
251 against flagellated bacteria, we utilized D90 d-ALOs due to its simpler cell
252 composition. Stimulation with PAO1-derived flagellin (FLA-PA) induced significant
253 upregulation of inflammatory mediators, including IL-6, CXCL8, CXCL10, and TNF-
254 α (Extended Data Fig. 7f). This response was substantially attenuated by the TLR5-
255 specific inhibitor TH1020 (Fig. 4d). To confirm that this response was specific to RAS
256 cells but not AT2 cells, we sorted AT2 cells using the HT2-280 antibody and found no
257 immune response to FLA-PA (Extended Data Fig. 7g-i). Furthermore, transplanted d-
258 ALOs demonstrated a TLR5-dependent inflammatory response to PAO1 infection (Fig.
259 4f). Taken together, these results establish that RAS cells orchestrate a robust TLR5
260 receptor-dependent inflammatory response to PAO1.

261 Clinical evidence highlights the pathological relevance of PAO1 lung colonization
262 in COPD[33]. To evaluate cytokine/chemokine secretion by RAS cells in human PAO1-
263 infected lungs, we analyzed tissue sections from COPD patients with PAO1 infection
264 (Fig. 4g). Immunostaining revealed increased co-expression of SFTPB, SCGB3A2, and

265 TLR5 in infected tissues compared to controls. Notably, CXCL8 and CXCL10 were
266 predominantly localized around RAS cells in infected lungs, implicating these cells in
267 driving localized inflammation. Together, these results indicate that RAS cells drive
268 immune responsiveness through TLR5 signaling both *in vitro* and *in vivo*.
269

270 **Discussion**

271 The distal respiratory airways have long eluded functional investigation due to their
272 anatomical inaccessibility and the inability of traditional rodent models to recapitulate
273 their biology. By establishing a hPSC-derived distal lung organoid system, we
274 overcome this challenge and uncover RAS cells as key immunoregulatory sentinels.
275 Single-cell transcriptomic profiling mapped the differentiation trajectory of RAS cells
276 from SOX9^{bright}NKX2-1^{bright} progenitors, demonstrating their multipotent capacity to
277 generate basal cells, PNECs, and AT2 cells. During RSV infection, RAS cells initiate
278 robust antiviral responses. Significantly, RAS cells display an extremely high
279 expression level of TLR5, and TLR5 activation triggers immune responses mirroring
280 pathological processes observed in COPD patients with PAO1 infection. Together, these
281 findings unveil a novel immunological role for RAS cells, endowing human distal
282 respiratory airways with unique defense mechanisms.

283 The evolutionary divergence between murine and human distal lung development
284 significantly limits our understanding of specialized cellular niches, as the human distal
285 lung contains far more branching generations and greater structural complexity of
286 airways than its murine counterparts[34,35]. Our work demonstrates that RAS cells derive

287 from SOX9^{bright}NKX2-1^{bright} bud tip progenitors and differentiate into AT2, basal, and
288 PNEC subtypes, marking them as key distal airway progenitors. Diseases such as
289 congenital pulmonary airway malformations (CPAM)[36] and bronchopulmonary
290 dysplasia (BPD)[37], which arise from developmental defects in small airway structures,
291 may stem from aberrant differentiation trajectories of these progenitors. Furthermore,
292 the plasticity of RAS cells evolved to support the structural repair and regeneration of
293 human distal respiratory airways[38,39]—initial site for gas exchange, which is enhanced
294 by an 8,000-fold greater surface area in humans compared to mice[35].

295 Acute viral and bacterial infections in the lower respiratory tract—extending from
296 respiratory bronchioles through alveolar ducts to alveolar sacs and alveoli—represent
297 major contributors to global morbidity and mortality[40]. Elucidating innate immune
298 mechanisms in the lower respiratory tract is critical for advancing our comprehension
299 of pulmonary infection pathogenesis and developing novel therapeutic interventions.
300 The distinctive cuboidal epithelium of human distal airways—characterized by absent
301 goblet cells and reduced ciliation—necessitates specialized defense mechanisms
302 divergent from proximal mucociliary clearance[41]. Our findings demonstrate that RAS
303 cells execute essential immune surveillance through dual antiviral and antibacterial
304 mechanisms. When challenged with RSV, the predominant etiological agent of infantile
305 bronchiolitis[42], RAS cells exhibit a remarkable antiviral response. This response
306 features significant upregulation of ISGs, effectively constraining viral replication and
307 dissemination through cell-autonomous immunity[43]. On the antibacterial front, RAS
308 cells display an intriguing characteristic—a uniquely high expression of TLR5. TLR5

309 is a key player in the innate immune system, as it recognizes bacterial flagellin, a protein
310 found in many pathogenic bacteria. The high expression of TLR5 in RAS cells allows
311 them to mount a potent immune response upon encountering flagellated bacteria such
312 as PAO1. Emerging research has established that mal-differentiation of SCGB3A2^{+}
313 secretory cell population in distal airways correlates with chronic pulmonary
314 pathologies including COPD and idiopathic pulmonary fibrosis (IPF)[13,14,44].
315 Importantly, our investigations reveal that RAS cells in COPD patients infected with
316 PAO1 displayed elevated chemokines secretion, providing valuable insights into the
317 pathophysiology of COPD and potentially opening new avenues for treatment.
318 Furthermore, comprehensive transcriptomic analysis identifies constitutive expression
319 of multifunctional host-defense effectors—including MUC1, SFTPB, and S100A6—in
320 resting RAS cells, underscoring their central role in maintaining pulmonary
321 homeostasis through integrated immunological functions.

322 Our study reveals a novel defense mechanism that has evolved to adapt to the
323 unique structure of the human respiratory airways. We provide a framework for
324 interpreting distal airway immune mechanisms by elucidating the origin, plasticity, and
325 defense functions of RAS cells. Further research should aim to unravel the role of RAS
326 cell immune function in the pathogenesis and progression of lung diseases, as well as
327 the corresponding therapeutic strategies targeting RAS cells.

328

329 **References**

330 1 Hewitt, R. J. & Lloyd, C. M. Regulation of immune responses by the airway
331 epithelial cell landscape. *Nat Rev Immunol* **21**, 347-362, doi:10.1038/s41577-020-
332 00477-9 (2021).

2 Mettelman, R. C., Allen, E. K. & Thomas, P. G. Mucosal immune responses to infection and vaccination in the respiratory tract. *Immunity* **55**, 749-780, doi:10.1016/j.immuni.2022.04.013 (2022).

3 Sadikot, R. T., Blackwell, T. S., Christman, J. W. & Prince, A. S. Pathogen-host interactions in Pseudomonas aeruginosa pneumonia. *Am J Respir Crit Care Med* **171**, 1209-1223, doi:10.1164/rccm.200408-1044SO (2005).

4 Weibel, E. R., Sapoval, B. & Filoche, M. Design of peripheral airways for efficient gas exchange. *Respir Physiol Neurobiol* **148**, 3-21, doi:10.1016/j.resp.2005.03.005 (2005).

5 Weibel, E. R. & Gomez, D. M. Architecture of the human lung. Use of quantitative methods establishes fundamental relations between size and number of lung structures. *Science* **137**, 577-585, doi:10.1126/science.137.3530.577 (1962).

6 Burgel, P. R. *et al.* Update on the roles of distal airways in COPD. *Eur Respir Rev* **20**, 7-22, doi:10.1183/09059180.10010610 (2011).

7 Booth, S. *et al.* A Single-Cell Atlas of Small Airway Disease in Chronic Obstructive Pulmonary Disease: A Cross-Sectional Study. *Am J Respir Crit Care Med* **208**, 472-486, doi:10.1164/rccm.202303-0534OC (2023).

8 Vannan, A. *et al.* Spatial transcriptomics identifies molecular niche dysregulation associated with distal lung remodeling in pulmonary fibrosis. *Nat Genet*, doi:10.1038/s41588-025-02080-x (2025).

9 Stancil, I. T. *et al.* Pulmonary fibrosis distal airway epithelia are dynamically and structurally dysfunctional. *Nat Commun* **12**, 4566, doi:10.1038/s41467-021-24853-8 (2021).

10 Rendeiro, A. F. *et al.* The spatial landscape of lung pathology during COVID-19 progression. *Nature* **593**, 564-569, doi:10.1038/s41586-021-03475-6 (2021).

11 Flerlage, T., Boyd, D. F., Meliopoulos, V., Thomas, P. G. & Schultz-Cherry, S. Influenza virus and SARS-CoV-2: pathogenesis and host responses in the respiratory tract. *Nat Rev Microbiol* **19**, 425-441, doi:10.1038/s41579-021-00542-7 (2021).

12 Sikkema, L. *et al.* An integrated cell atlas of the lung in health and disease. *Nat Med* **29**, 1563-1577, doi:10.1038/s41591-023-02327-2 (2023).

13 Basil, M. C. *et al.* Human distal airways contain a multipotent secretory cell that can regenerate alveoli. *Nature* **604**, 120-126, doi:10.1038/s41586-022-04552-0 (2022).

14 Kadur Lakshminarasimha Murthy, P. *et al.* Human distal lung maps and lineage hierarchies reveal a bipotent progenitor. *Nature* **604**, 111-119, doi:10.1038/s41586-022-04541-3 (2022).

15 Cao, S. *et al.* Single-cell RNA sequencing reveals the developmental program underlying proximal-distal patterning of the human lung at the embryonic stage. *Cell Res* **33**, 421-433, doi:10.1038/s41422-023-00802-6 (2023).

16 Morrisey, E. E. & Hogan, B. L. Preparing for the first breath: genetic and cellular mechanisms in lung development. *Dev Cell* **18**, 8-23, doi:10.1016/j.devcel.2009.12.010 (2010).

17 Minoo, P., Su, G., Drum, H., Bringas, P. & Kimura, S. Defects in tracheoesophageal and lung morphogenesis in Nkx2.1(-/-) mouse embryos. *Dev Biol* **209**, 60-71, doi:10.1006/dbio.1999.9234 (1999).

18 Kelly, S. E., Bachurski, C. J., Burhans, M. S. & Glasser, S. W. Transcription of the lung-specific surfactant protein C gene is mediated by thyroid transcription factor 1. *J Biol Chem* **271**, 6881-6888, doi:10.1074/jbc.271.12.6881 (1996).

19 Lim, K. *et al.* Organoid modeling of human fetal lung alveolar development reveals mechanisms of cell fate patterning and neonatal respiratory disease. *Cell Stem Cell* **30**, 20-37 e29, doi:10.1016/j.stem.2022.11.013 (2023).

20 Miller, A. J. *et al.* Generation of lung organoids from human pluripotent stem cells in vitro. *Nat Protoc* **14**, 518-540, doi:10.1038/s41596-018-0104-8 (2019).

21 Crespo, M. *et al.* Colonic organoids derived from human induced pluripotent stem cells for modeling colorectal cancer and drug testing. *Nat Med* **23**, 878-884, doi:10.1038/nm.4355 (2017).

22 Vazquez-Armendariz, A. I. & Tata, P. R. Recent advances in lung organoid development and applications in disease modeling. *J Clin Invest* **133**, doi:10.1172/JCI170500 (2023).

23 McCauley, K. B. *et al.* Efficient Derivation of Functional Human Airway Epithelium from Pluripotent Stem Cells via Temporal Regulation of Wnt Signaling. *Cell Stem Cell* **20**, 844-857 e846, doi:10.1016/j.stem.2017.03.001 (2017).

24 Yamamoto, Y. *et al.* Long-term expansion of alveolar stem cells derived from human iPS cells in organoids. *Nat Methods* **14**, 1097-1106, doi:10.1038/nmeth.4448 (2017).

25 Co, J. Y. *et al.* Controlling Epithelial Polarity: A Human Enteroid Model for Host-Pathogen Interactions. *Cell Rep* **26**, 2509-2520 e2504, doi:10.1016/j.celrep.2019.01.108 (2019).

26 Travaglini, K. J. *et al.* A molecular cell atlas of the human lung from single-cell RNA sequencing. *Nature* **587**, 619-625, doi:10.1038/s41586-020-2922-4 (2020).

27 Conchola, A. S. *et al.* Regionally distinct progenitor cells in the lower airway give rise to neuroendocrine and multiciliated cells in the developing human lung. *Proc Natl Acad Sci U S A* **120**, e2210113120, doi:10.1073/pnas.2210113120 (2023).

28 Sountoulidis, A. *et al.* A topographic atlas defines developmental origins of cell heterogeneity in the human embryonic lung. *Nat Cell Biol* **25**, 351-365, doi:10.1038/s41556-022-01064-x (2023).

29 Pickles, R. J. & DeVincenzo, J. P. Respiratory syncytial virus (RSV) and its propensity for causing bronchiolitis. *J Pathol* **235**, 266-276, doi:10.1002/path.4462 (2015).

30 Liesman, R. M. *et al.* RSV-encoded NS2 promotes epithelial cell shedding and distal airway obstruction. *J Clin Invest* **124**, 2219-2233, doi:10.1172/JCI72948 (2014).

31 Kovach, M. A. & Standiford, T. J. Toll like receptors in diseases of the lung. *Int Immunopharmacol* **11**, 1399-1406, doi:10.1016/j.intimp.2011.05.013 (2011).

32 Quach, H. *et al.* Early human fetal lung atlas reveals the temporal dynamics of epithelial cell plasticity. *Nat Commun* **15**, 5898, doi:10.1038/s41467-024-50281-5 (2024).

33 Qin, S. *et al.* Pseudomonas aeruginosa: pathogenesis, virulence factors, antibiotic resistance, interaction with host, technology advances and emerging therapeutics. *Signal Transduct Target Ther* **7**, 199, doi:10.1038/s41392-022-01056-1 (2022).

34 Pan, H., Deutsch, G. H., Wert, S. E., Ontology, S. & Consortium, N. M. A. o. L. D. P.

Comprehensive anatomic ontologies for lung development: A comparison of alveolar formation and maturation within mouse and human lung. *J Biomed Semantics* **10**, 18, doi:10.1186/s13326-019-0209-1 (2019).

35 Basil, M. C. & Morrisey, E. E. Lung regeneration: a tale of mice and men. *Semin Cell Dev Biol* **100**, 88-100, doi:10.1016/j.semcdb.2019.11.006 (2020).

36 Jiang, Y. *et al.* Alteration of cystic airway mesenchyme in congenital pulmonary airway malformation. *Sci Rep* **9**, 5296, doi:10.1038/s41598-019-41777-y (2019).

37 Bhandari, A. & McGrath-Morrow, S. Long-term pulmonary outcomes of patients with bronchopulmonary dysplasia. *Semin Perinatol* **37**, 132-137, doi:10.1053/j.semperi.2013.01.010 (2013).

38 Beers, M. F. & Morrisey, E. E. The three R's of lung health and disease: repair, remodeling, and regeneration. *J Clin Invest* **121**, 2065-2073, doi:10.1172/JCI45961 (2011).

39 Hogan, B. L. *et al.* Repair and regeneration of the respiratory system: complexity, plasticity, and mechanisms of lung stem cell function. *Cell Stem Cell* **15**, 123-138, doi:10.1016/j.stem.2014.07.012 (2014).

40 Lipscomb, M. F., Hutt, J., Lovchik, J., Wu, T. & Lyons, C. R. The pathogenesis of acute pulmonary viral and bacterial infections: investigations in animal models. *Annu Rev Pathol* **5**, 223-252, doi:10.1146/annurev-pathol-121808-102153 (2010).

41 Hoytema van Konijnenburg, D. P., Nigrovic, P. A. & Zanoni, I. Regional specialization within the mammalian respiratory immune system. *Trends Immunol* **45**, 871-891, doi:10.1016/j.it.2024.09.011 (2024).

42 Florin, T. A., Plint, A. C. & Zorc, J. J. Viral bronchiolitis. *Lancet* **389**, 211-224, doi:10.1016/S0140-6736(16)30951-5 (2017).

43 Schneider, W. M., Chevillotte, M. D. & Rice, C. M. Interferon-stimulated genes: a complex web of host defenses. *Annu Rev Immunol* **32**, 513-545, doi:10.1146/annurev-immunol-032713-120231 (2014).

44 Pezet, M. G. *et al.* Human respiratory airway progenitors derived from pluripotent cells generate alveolar epithelial cells and model pulmonary fibrosis. *Nat Biotechnol*, doi:10.1038/s41587-025-02569-0 (2025).

45 Chen, L. *et al.* Directed differentiation of pancreatic delta cells from human pluripotent stem cells. *Nat Commun* **15**, 6344, doi:10.1038/s41467-024-50611-7 (2024).

46 Meng, H. *et al.* FGF7 enhances the expression of ACE2 in human islet organoids aggravating SARS-CoV-2 infection. *Signal Transduct Target Ther* **9**, 104, doi:10.1038/s41392-024-01790-8 (2024).

47 Stokes, K. L. *et al.* Differential pathogenesis of respiratory syncytial virus clinical isolates in BALB/c mice. *J Virol* **85**, 5782-5793, doi:10.1128/JVI.01693-10 (2011).

48 Moore, M. L. *et al.* A chimeric A2 strain of respiratory syncytial virus (RSV) with the fusion protein of RSV strain line 19 exhibits enhanced viral load, mucus, and airway dysfunction. *J Virol* **83**, 4185-4194, doi:10.1128/JVI.01853-08 (2009).

49 Sun, J. *et al.* Transplantation of hPSC-derived pericyte-like cells promotes functional recovery in ischemic stroke mice. *Nat Commun* **11**, 5196, doi:10.1038/s41467-020-19042-y (2020).

465 **Methods**

466 **Human Pluripotent Stem Cell Culture**

467 The H1 and H9 human embryonic stem cell lines (hESC) and UE005 human induced
468 pluripotent stem cell line (hiPSC) were maintained on Matrigel-coated 6-well plates
469 (Corning, 354277) in mTeSR1 medium (StemCell Technologies, 85850). Cells were
470 cultured under mycoplasma-free conditions, with daily medium replacement. At ~80%
471 confluency (typically every 4–5 days), cells were passaged as small clusters using 0.5
472 mM EDTA.

473 **Differentiation of Lung Progenitors from hPSCs**

474 For differentiation, human pluripotent stem cells were dissociated into single cells using
475 Accutase (StemCell Technologies, 07920), resuspended in mTeSR1 medium
476 supplemented with 10 μM Y27632 (MCE, HY-10071), and counted using an automated
477 cell counter (HUAPO AP-CFcount300) with Trypan blue (Gibco; 1:1 ratio) for viability
478 assessment. Single cells were seeded at 1×10^5 cells/well on Matrigel-coated 24-well
479 plates and maintained in mTeSR1 medium with Y27632. After 24 hours, medium was
480 replaced with ncTarget medium (nuwacell, RP01020) without Y27632. Daily medium
481 changes were performed until differentiation initiation at ~70% confluency (normally
482 48 hours post-seeding). Definitive endoderm differentiation (day 0) followed
483 established protocols [45,46]. Cells were treated with 100 ng/ml activin A (MCE, HY-
484 P70311) in MCDB131 medium (Reprocell, PM151210) and stepwise reductions of
485 CHIR99021 (MCE, HY-10182; 3 μM on day 0, 0.3 μM on day 1, none on day 2).
486 After DE specification, cells were cultured for 5 days in Advanced DMEM/F12 (Gibco,

487 12634028) containing 1× GlutaMax (Gibco, 35050061), 10 mM HEPES (Thermo
488 Fisher, 15630080) and Penicillin/Streptomycin (Gibco, 15070063), 1× B27 supplement
489 (Gibco, 17504044), 1× N2 supplement (Gibco, 17502048), 500 ng/ml FGF4 (MCE,
490 HY-P7014), 200 ng/ml noggin (MCE, HY-P7051A), 2 μM CHIR99021, 10 μM
491 SB431542 (MCE, HY-10431) and 1 μM SAG (MCE, HY-12848). Detached anterior
492 foregut spheroids (days 5–7) were split into two groups:

493 1. p-LO: Spheroids were embedded in growth factor-reduced Matrigel (Corning,
494 354230) and cultured in LPC medium (20 ng/ml BMP4 [MCE, HY-P7007], 10 ng/ml
495 FGF7/KGF [MCE, HY-P70597], 10 ng/ml FGF10 [MCE, HY-P70695], 3 μM
496 CHIR99021, 20 μM DAPT [MCE, HY-13027], and 50 nM retinoic acid [Sigma,
497 R2625]).

498 2. d-LO: Spheroids were washed with PBS, dissociated into single cells with
499 Accutase, pelleted (300 × g, 5 min), and resuspended in growth factor-reduced Matrigel.
500 After solidification (37°C, 15 min), cultures were maintained in LPC medium with 10
501 μM Y27632.

502 Medium from both groups was refreshed every 48 hr for 7 days to induce lung
503 progenitor differentiation.

504 **Airway and Alveolar Differentiation**

505 *Human Lung Organoid (HLO) Differentiation Medium*

506 HLO differentiation basal medium comprised Advanced DMEM/F12 supplemented
507 with 2.5% BSA (Proliant, 69760), 100 U/ml penicillin-streptomycin, 1× GlutaMax, 1×
508 B27, and ITS-X (Reprocell, pb180431).

509 *Airway Differentiation*

510 Lung organoids were cultured in airway (DCIK) differentiation medium (HLO
511 differentiation basal medium supplemented with 50 nM dexamethasone [MCE, HY-
512 14648], 100 nM 8-bromo-cAMP [MCE, HY-12306], 100 nM 3-Isobutyl-1-
513 methylxanthine [IBMX; MCE, HY-12318] and 10 ng/ml KGF) with medium changes
514 every 48 hr.

515 *Alveolar Differentiation*

516 Lung organoids were cultured in alveolar (DCIK+CSB) differentiation medium (HLO
517 differentiation basal medium supplemented with DCIK, 3 μM CHIR99021 and 10 μM
518 SB431542) with medium changes every 48 hr.

519 **Histology and immunostainings**

520 Formalin-fixed, paraffin-embedded human distal lung tissue sections (obtained from
521 resections at the First Affiliated Hospital of Guangzhou Medical University, China)
522 were dewaxed, rehydrated, and subjected to antigen retrieval using Improved Citrate
523 Antigen Retrieval Solution (Beyotime, P0083) in a 95°C water bath for 15 min.
524 Sections were washed with PBS, permeabilized and blocked using QuickBlock™
525 Blocking Buffer for Immunol Staining (Beyotime, P0260) for at least 15 min at room
526 temperature (RT), followed by incubation with primary antibodies at 4 °C overnight.
527 Sections were washed with 0.1% Triton X-100 in PBS (PBST), incubated with species-
528 matched Alexa Fluor-conjugated secondary antibodies (1:1,000; Thermo Fisher
529 Scientific) for 2 hr at RT, counterstained with Hoechst 33342 (1:1,000, Thermo
530 Scientific, 62249), and mounted with fluorescence mounting medium (DAKO, S3023).

531 Images were acquired using a Zeiss LSM980 confocal microscope.

532 For whole-mount staining, organoids were extracted from Matrigel using Cell
533 Recovery Solution (Corning, 354253), fixed in 4% paraformaldehyde (PFA) for 2 hr at
534 4°C, permeabilized, and stained as above. Primary antibodies used were rabbit anti-
535 NKX2-1 (1:300, Abcam, ab76013), goat anti-SOX2 (1:300, Abcam, ab239218), mouse
536 anti-SOX9 (1:500, Abcam, ab76997), mouse anti-Ac-Tub (1:1000, Sigma-Aldrich,
537 T7451), rabbit anti-TP63 (1:200, Abcam, ab124762), mouse anti-VIM (1:100, Santa
538 Cruz Biotechnology, sc-6260), mouse anti-SFTPB (1:200, Santa Cruz Biotechnology,
539 sc-133143), goat anti-SCGB3A2 (1:500, Invitrogen, M801), mouse anti-MUC5AC
540 (1:500, Abcam, ab3649), rabbit anti-SFTPC (1:200, Seven Hills Bioreagents, WRAB-
541 9337), goat anti-AGER (1:200, R&D Systems, AF1145), rabbit anti-TLR5 (1:500,
542 abcam, ab300038), mouse anti-HUNU (1:300, Abcam, ab191181), rabbit anti-CXCL10
543 (1:100, Invitrogen, MA532674), mouse anti-CXCL8 (1:500, Invitrogen, M801), rabbit
544 anti-RSV-F (1:200, Sino Biological, 11049-R302). Organoids were incubated with
545 Alexa Fluor 647 phalloidin (1:1000, Thermo Fisher Scientific, A22287), with the
546 corresponding secondary antibodies Alexa Fluor 488 Donkey anti-Rabbit (Thermo
547 Fisher Scientific, A21206), Alexa Fluor 546 Donkey anti-Rabbit (Thermo Fisher
548 Scientific, A10040), Alexa Fluor 488 Donkey anti-Mouse (Thermo Fisher Scientific,
549 A21202), Alexa Fluor 546 Donkey anti-Mouse (Thermo Fisher Scientific, A10036),
550 Alexa Fluor 405 Donkey anti-Goat (Thermo Fisher Scientific, A48259), Alexa Fluor
551 647 Donkey anti-Goat (Thermo Fisher Scientific, A21447) in blocking buffer
552 containing Hoechst 33342 solution (20 mM) (1:1,000). Organoids were transferred to

553 a confocal dish, and images were acquired using the Zeiss LSM980 confocal
554 microscope.

555 **RSV Infection of Organoids**

556 RSV strain Long was propagated as described [47,48]. d-ALOs were infected at a
557 multiplicity of infection (MOI) of 0.1 for 2 hours at 37°C. Organoids were washed three
558 times with DPBS (Hyclone, AH30017338) and cultured in fresh alveolar medium for
559 24–72 hours. Organoids and supernatants were collected at designated time points for
560 downstream analysis.

561 **Assessment of Cytokine Production**

562 To evaluate cytokine secretion, d-ALOs were treated with varying concentrations of
563 FLA-PA (InvivoGen, tlrl-pafla). Supernatants were collected at designated timepoints,
564 aliquoted, and stored at −80°C until batch analysis. Cytokine levels were quantified
565 using a magnetic Luminex® multiplex assay (R&D Systems, LXSAHM-08) according
566 to the manufacturer's instructions. Briefly, serial dilutions of cytokine standards were
567 prepared. Antibody magnetic bead mix was dispensed into a 96-well plate, followed by
568 the addition of standards and experimental samples. The plate was incubated overnight
569 at 4°C with shaking. After three washes, detection antibodies were introduced and
570 incubated at RT for 30 minutes with shaking. The plate was washed three times.
571 Streptavidin-PE was subsequently added and incubated under identical conditions.
572 Following a final wash cycle, 100 μl of wash buffer was dispensed into each well.
573 Fluorescence intensity was measured using a Luminex X-200 system, and acquired data
574 were processed with Milliplex Analyst software (v5.1).

575 **Mouse Kidney Capsule Transplantation**

576 All animal procedures were approved by the Institutional Animal Care and Use
577 Committee of Guangzhou National Laboratory and conducted in accordance with
578 institutional guidelines. NOD.Cg-*Prkdc*^{scid}*Il2rg*^{em1}/Smoc (NSG) mice (8-10 weeks old;
579 Shanghai Model Organisms Center, NM-NSG-001) were housed under specific
580 pathogen-free conditions. d-ALO cells mixed with 5 μL Matrigel were implanted
581 beneath the right kidney capsule under anesthesia. At 4 weeks post-transplantation,
582 grafts were excised, fixed in 4% PFA overnight, dehydrated in 30% sucrose overnight,
583 and embedded in Optimal Cutting Temperature (OCT) compound or paraffin for
584 immunofluorescence or hematoxylin and eosin (H&E) staining, respectively.

585 For bacterial infection, PAO1 (MiaoLingBio, T0133) was cultured overnight in
586 LB medium at 37°C with shaking. The bacterial suspension was centrifuged, washed
587 three times with PBS, and resuspended in sterile saline to an optical density OD600 of
588 1.0, corresponding to 1×10^9 colony-forming units (CFU) per mL. For experimental
589 use, the suspension was diluted to 1×10^6 CFU/mL, pelleted by centrifugation (10,000
590 × g, 5 min, 4°C), and subjected to four freeze-thaw cycles to achieve bacterial lysis.
591 At 4 weeks post-transplantation, mice were anesthetized and a posterior left incision
592 was made to expose the engrafted d-ALO. A 50 μL aliquot of PAO1 lysate was injected
593 into the d-ALO lumen using a sterile 0.5-mL insulin syringe. The d-ALO was
594 repositioned into the peritoneal cavity, and the incision was closed via a two-layer
595 suturing technique. For pain control, mice were given an injection with carprofen
596 subcutaneously (4 mg/kg, Zoetis). At 48 hours post-injection, mice were euthanized.

597 Engrafted d-ALO tissues and adjacent kidney samples were harvested for subsequent
598 analysis.

599 **RNA Isolation and qPCR**

600 Total RNA was extracted using the RNeasy Kit (Qiagen, 74106) following the
601 manufacturer's instructions. qPCR was performed using Bio-Rad CFX384 Real-Time
602 PCR Detection System, with primers listed in Supplementary Table 1. Biological and
603 technical replicates were analyzed as previously described[49].

604 **Flow Cytometry**

605 Lung organoids were dissociated into single cells using TrypLE (Gibco, 12605028) at
606 37°C. For AT2 sorting, cells were stained 30 mins with primary antibody (mouse anti-
607 HTII-280 [1:150, TerraceBiotech, TB-27AHT2-280]) at 4°C, followed by secondary
608 antibody incubation (45 minutes, RT). Cells were sorted using Sony MA900 Cell Sorter.
609 For NKX2-1 assessment, after dissociation, cells were fixed in 1% PFA for 15 minutes
610 at 4°C, and permeabilized with 1× Perm/Wash Buffer (BD Biosciences, 554723) for
611 20 minutes at RT. Cells were stained under identical condition using anti-NKX2-1
612 antibody (1:300, Abcam, ab76013) and analyzed by Beckman CytoFLEX S flow
613 cytometer. Data were analyzed using FlowJo v10.6.2. or CytExpert.

614 **Forskolin-Induced Organoid Swelling**

615 d-AWOs at day 35–45 were used for swelling assays. Prior to treatment, organoids were
616 passaged into 3 μL growth factor-reduced Matrigel droplets and cultured in the absence
617 of 8-bromo-cAMP and IBMX for at least one day. For swelling analysis, organoids
618 were incubated with 10 mM forskolin (Aladdin Scientific, F127328-500mg) in fresh

619 medium for 5–24 hours at 37°C under 5% CO_2. Brightfield images of entire droplets
620 were captured at 0, 5, 7, and 24 hours post-treatment using a High-Content Imaging
621 System (PerkinElmer, Operetta CLS) and stitched with Harmony software. Swelling
622 area ratios (post-treatment area / baseline area) were quantified in ImageJ from replicate
623 wells, with the initial area (t = 0) normalized to 1. Statistical analyses included 20
624 organoids per experimental replicate.

625 **Transmission Electron microscopy**

626 d-ALOs were fixed in 2.5% glutaraldehyde for 30 minutes at RT, washed with 0.1 M
627 phosphate buffer (pH 7.4), and postfixed in 1% osmium tetroxide for 1.5 hours at RT.
628 After repeated phosphate buffer washes, samples were dehydrated in a graded ethanol
629 series (50%, 70%, 80%, 90%, 100%) at RT. Tissues were infiltrated with propylene
630 oxide, followed by a 1:1 propylene oxide/Epon mixture (2–4 hours, RT), then pure
631 Epon resin (1 hour, RT). Samples were embedded in Epon resin, polymerized at 40°C
632 (24 hours) and 60°C (12 hours), and sectioned (70–90 nm). Ultrathin sections were
633 stained with uranyl acetate and lead citrate and imaged on a FEI Tecnai Transmission
634 Electron Microscope.

635 **Live-Cell Imaging of Lamellar Bodies**

636 d-ALOs were incubated with β-BODIPY FL C12-HPC (1 μM; Life Technologies,
637 D3792) in alveolar differentiation medium for 24 hours at 37°C/5% CO_2. Organoids
638 were washed and stained with LysoTracker Red DND-99 (100 nM; Life Technologies,
639 L7528) for 30 min at RT, followed by two washes. Live imaging was performed at 37°C
640 using a Zeiss LSM980 confocal microscope.

641 **Organoid scRNA-seq**

642 *Sample Preparation and Library Construction*

643 Single-cell suspensions were generated from lung organoids, and viability was assessed
644 using a Luna Dual Fluorescence Cell Counter. Libraries were prepared with the
645 Chromium Single Cell 3′ Library and Gel Bead Kit v3 (10x Genomics) following the
646 manufacturer's protocol. Briefly, single-cell suspensions were loaded into a Chromium
647 Controller to produce Gel Bead-in-Emulsions (GEMs). Following reverse transcription,
648 cDNA amplification, and library construction, sequencing was performed on an
649 Illumina NovaSeq 6000 platform (PE150; Annoroad Gene Technology).

650 *Data Preprocessing*

651 Raw sequencing data were processed via the Cell Ranger pipeline (v4.0.0). Reads were
652 aligned to the GRCh38 human genome, and gene expression matrices were generated.
653 Low-quality cells (fewer than 500 detected genes or >10% mitochondrial genes) were
654 excluded. Doublets were identified and removed using DoubletFinder (v2.0.4).

655 *Data Analysis with Seurat*

656 The filtered gene expression matrix was analyzed using the Seurat (v5.1.0). After
657 quality control, the datasets were merged independently using the 'Seurat::merge()'
658 function. Data normalization was performed using the "NormalizeData" function with
659 a scale factor of 10,000. Highly variable genes were identified using the
660 "FindVariableFeatures" function, and the data were scaled using the "ScaleData"
661 function. Principal Component Analysis (PCA) was conducted to reduce dimensionality.
662 Batch effects were then corrected by integrating the data using the "Harmony" method.

Cells were clustered using the "FindNeighbors" and "FindClusters" functions. The clusters were visualized using Uniform Manifold Approximation and Projection (UMAP) with the "RunUMAP" function. Marker genes for each cluster were identified using the "FindAllMarkers" function with a log-fold change threshold of 0.25.

Cell-Type Annotation

Cell type annotation was performed by identifying cluster-specific genes using the "FindAllMarkers" function. The resulting cluster markers were then cross-referenced with a curated list of known cell type markers to assign cell identities accurately.

Differential Expression and Pathway Analysis

Differentially expressed genes (DEGs) between clusters were identified using the "FindMarkers" function, calculating fold change and performing Wilcoxon Rank Sum tests. Gene Ontology (GO) and pathway enrichment analyses were performed using clusterProfiler (v4.14.4) to interpret the biological significance of the identified markers.

Trajectory Inference Analysis

Trajectory analysis was conducted using Monocle3 (v1.3.7). The UMAP coordinates obtained from Seurat were utilized as the input for Monocle3 to construct the trajectory. Cells were ordered along the pseudotime trajectory based on the learned principal graph, allowing for the identification of dynamic gene expression changes across different stages of the trajectory.

Statistical analysis

Statistical tests (one-way ANOVA, two-way ANOVA, unpaired Student’s t-test) were performed in GraphPad Prism (v8.0.2). Data represent biologically independent

replicates (≥3 experiments, except scRNA-seq). Results are expressed as mean ± SEM. All tests were two-sided ($\alpha = 0.05$).

Data availability

Organoid and primary tissue scRNA-seq data that support the findings of this study were deposited in the Gene Expression Omnibus under accession code GSE292679, and are publicly available.

Code availability

Custom code and scripts used to analyse the data and produce the figures are available in a public GitHub repository (https://github.com/jiangjasson/lung-organoids-analysis).

Acknowledgements This work was supported by grants from the National Natural Science Foundation of China (82171419), the National Key Research and Development Program of China (2021YFA1101304, 2020YFA0908200)

Author contributions J.S. conceptualized and supervised the project, designed and performed experiments, interpreted the results and wrote the paper. H.S. performed experiments and analysis. S.J. performed scRNA-seq analysis. X.X. performed mouse kidney capsule transplantation. D.W. performed RSV infection experiments. H.Y. and W.G. provided constructs. J.Z. supervised and supported RSV infection experiments. W.K.Z. supervised scRNA-seq work and analysis. H.L. and T.X. supervised the

research. H.L. edited the paper.

Competing interests The authors declare no competing interests.

Correspondence and requests for materials should be addressed to Huisheng Liu.

Figures

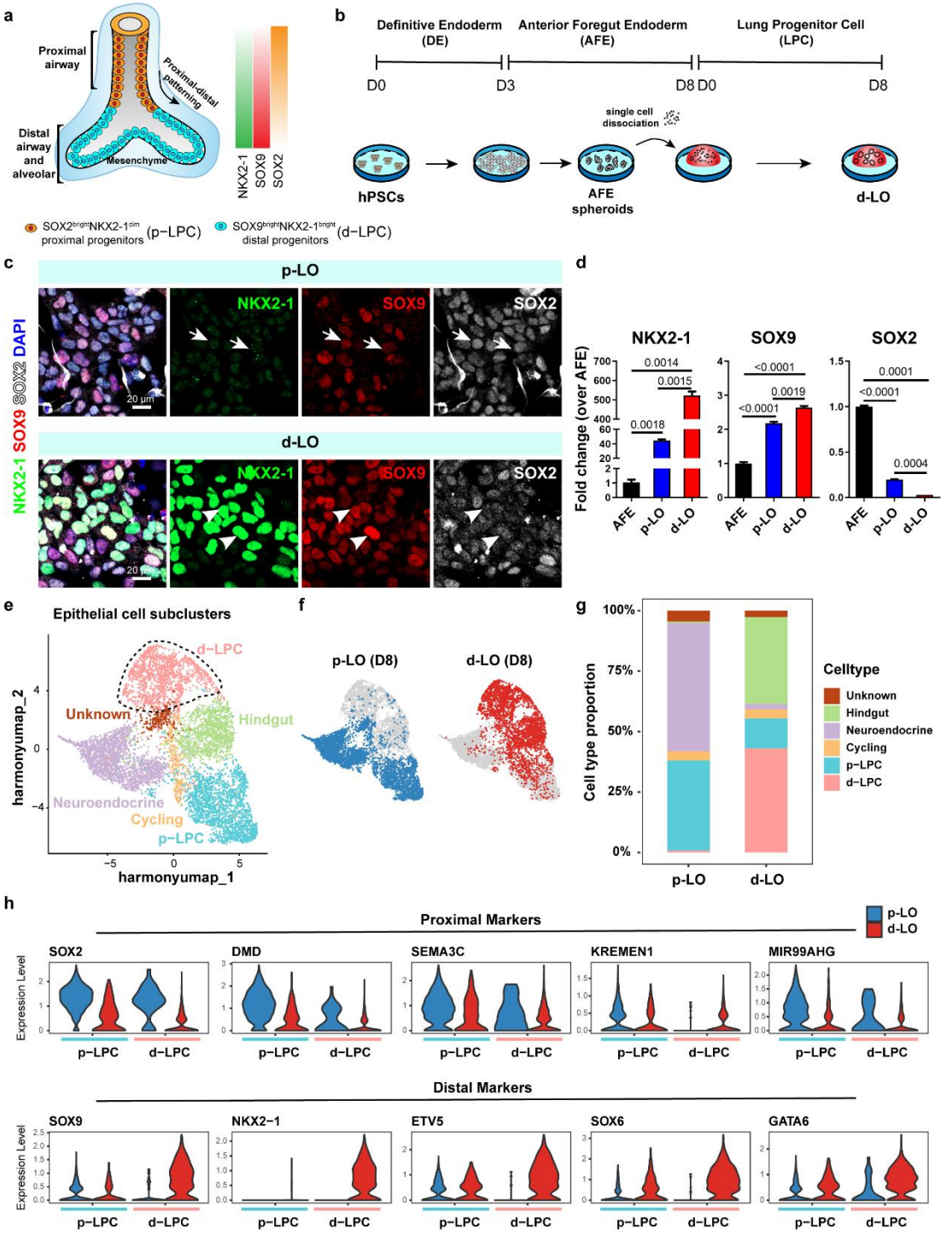

Fig. 1 Robust induction of distal lung progenitor cells through AFE spheroid dissociation. a, Schematic of proximal-distal patterning in developing human lung with representative lineage markers. **b**, Differentiation protocol workflow from human pluripotent stem cells (hPSCs) to distal lung organoids (d-LOs) via anterior foregut

721 endoderm (AFE) spheroids dissociation. **c**, Immunofluorescence staining of NKX2-1,
722 SOX2 and SOX9 in proximal (p-LO) and distal (d-LO) lung organoids at day 8. White
723 arrows denote SOX2^{bright}NKX2-1^{dim} cells; arrowheads indicate SOX9^{bright}NKX2-1^{bright}
724 cells. Scale bars, 20 μm. Representative images from three biologically independent
725 experiments. **d**, Quantitative PCR analysis of *NKX2-1*, *SOX9* and *SOX2* expression in
726 AFE spheroids, d-LOs and p-LOs. Data presented as mean ± s.e.m. (n=3 biological
727 replicates). *P*-values were calculated using two-tailed Student's *t*-test with Welch's
728 correction. **e**, UMAP with annotations of different cell types from epithelial cell
729 subclusters. **f**, Individual conditions of epithelial subclusters shown in (**e**). **g**,
730 Proportional distribution of cell types between d-LO and p-LO. **h**, Violin plots showing
731 expression levels of proximal and distal markers in p-LPC and d-LPC cell populations
732 from d-LO and p-LO.
733
734
735
736
737
738

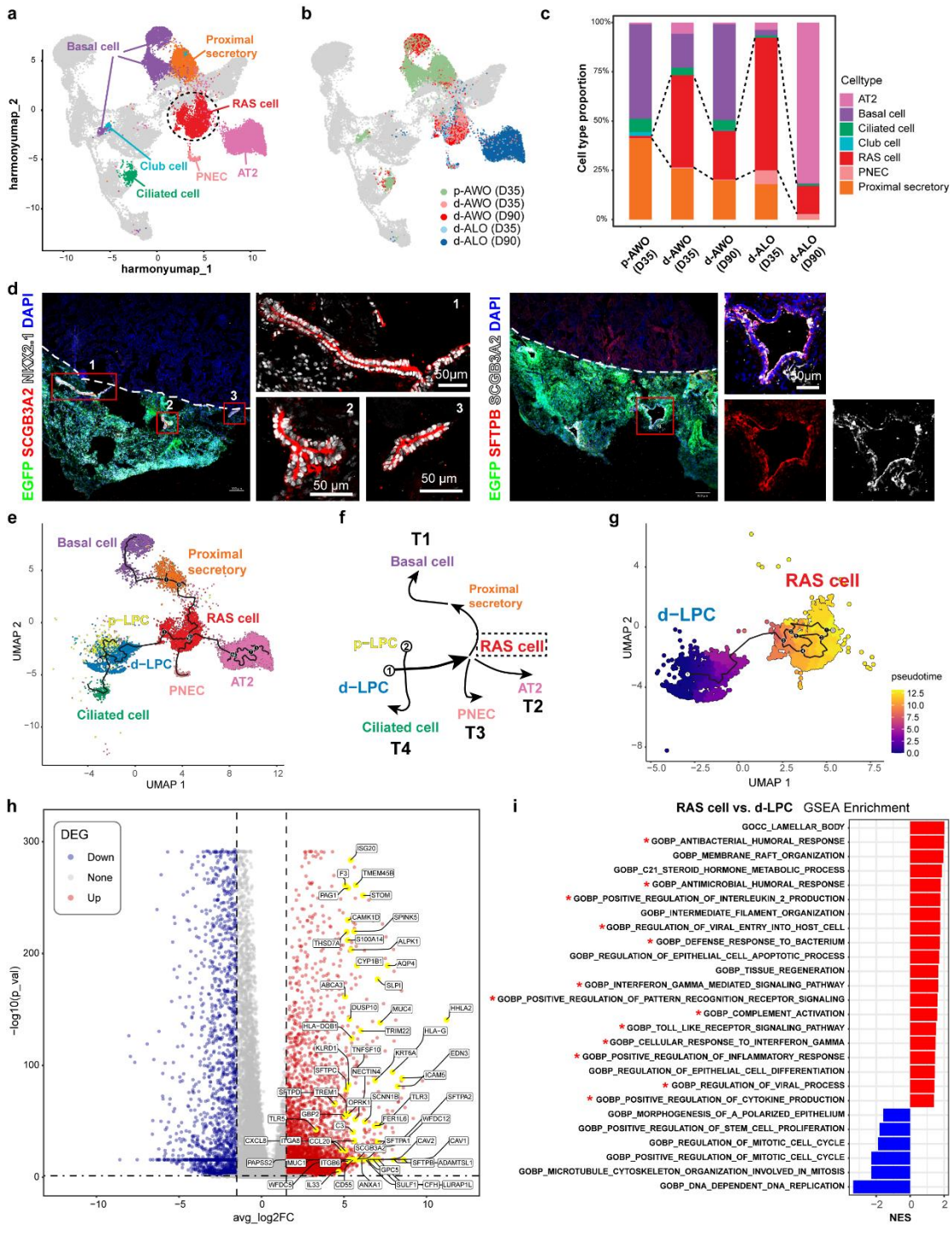

Fig. 2 Developmental trajectories and functional characterization of RAS cells. a,**b**, Single-cell RNA sequencing analysis of p-LO- and d-LO-derived organoids. UMAP embeddings colored by annotated cell types (**a**) or differentiation time/media conditions (**b**). **c**, Proportional cell type composition in d-LO- and p-LO-derived organoids. **d**, Immunofluorescence imaging of transplanted d-ALOs at 4 weeks post-engraftment.

745 Triple staining for SCGB3A2 (red), EGFP (green), and NKX2-1 (grey) (left); SFTPB
746 (red), EGFP (green), and SCGB3A2 (grey) (right). Scale bars, 100 μm (wide-field
747 images), 50 μm (magnified images). Representative images from three biologically
748 independent experiments. **e**, Pseudotemporal trajectory reconstruction of epithelial
749 subtypes using Monocle3. **f**, Schematic summarizing developmental lineages inferred
750 from (**e**). **g**, Differentiation trajectory connecting d-LPCs to RAS cells. **h**, Volcano plot
751 of differentially expressed genes (DEGs) between d-LPCs and RAS cells. **i**, Gene set
752 enrichment analysis (GSEA) of DEGs from (**h**), ranked by normalized enrichment score
753 (NES).
754
755
756
757
758
759
760
761
762
763
764
765
766

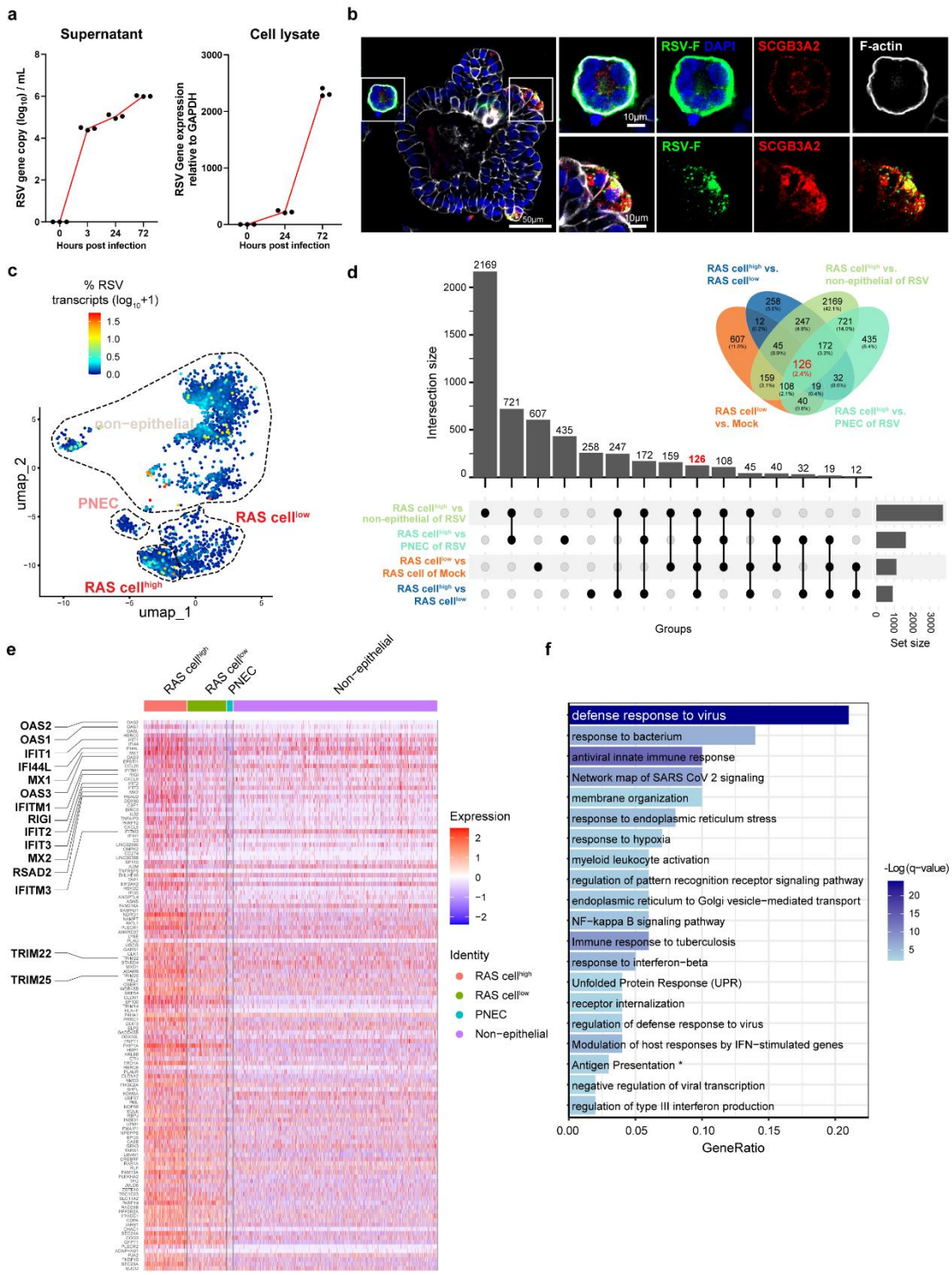

Fig. 3 Enhanced antiviral activity of RAS cells during RSV infection. a, RSV replication kinetics in d-ALOs quantified by RT–qPCR of viral RNA in supernatants (left) and cell lysates (right) at indicated time points. Each dot is a well. n = 3 biological replicates. **b**, Morphological changes in d-ALOs post-RSV infection. Left: overview;

right: magnified regions showing cytopathic effects. Scale bars, 50 μm (overview), 10 μm (magnified images). Representative of three independent experiments. **c**, UMAP projection of single-cell transcriptomes colored by percentage of viral transcripts per cell. **d**, Venn diagram comparing differentially expressed genes (DEGs) between RAS cells with high infection (RAS cell^{high}) versus the other clusters, and RAS cells with low infection (RAS cell^{low}) versus the same cluster in mock. **e**, Heatmap of 126 common DE genes across RSV-infected d-ALOs. **f**, Gene Ontology (GO) enrichment analysis of shared DE genes, highlighting "defense response to virus" as the top pathway. The full name of the term marked by an asterisk is 'Antigen Presentation: Folding, assembly and peptide loading of class I MHC'.

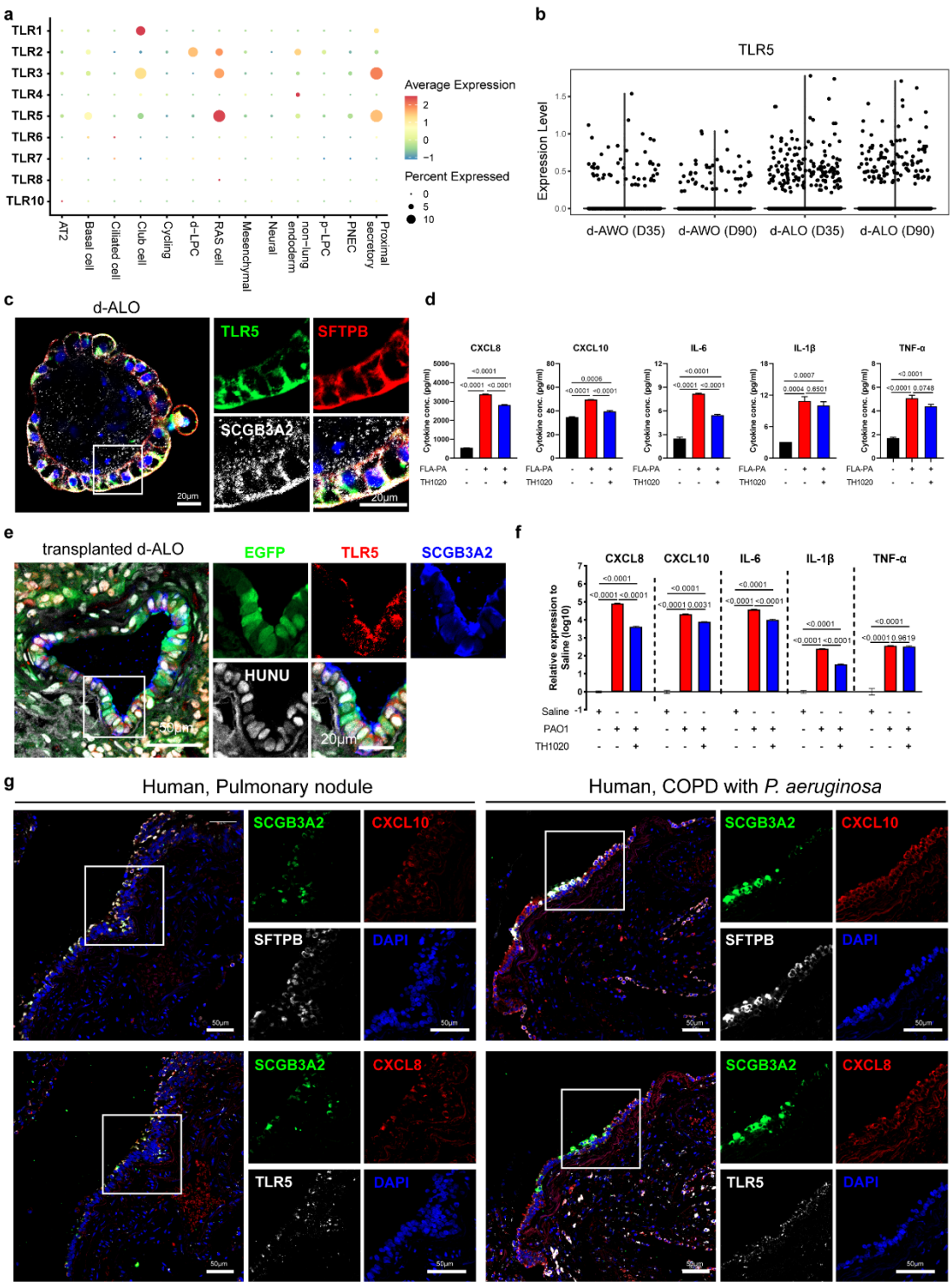

794

795 **Fig. 4 TLR5 activation mediates microbial-induced inflammatory responses in**

796 **RAS cells. a**, Expression of Toll-like receptors (TLRs) across all cell clusters (Extended

797 Data Fig. 5c). **b**, Violin plots comparing *TLR5* expression in RAS cells under indicated

798 experimental conditions. **c**, Whole-mount immunofluorescence of TLR5 (green) in

799 RAS cells (SFTPB, red and SCGB3A2, grey) in d-ALO. Nuclei counterstained with
800 Hoechst (blue). Scale bars, 20 μm. Representative of three independent experiments. **d**,
801 Cytokine/chemokine secretion (CXCL8, CXCL10, IL-6, IL-1β, TNF-α) from d-ALOs
802 stimulated with 1 μg/ml FLA-PA protein ± 1 μM TLR5 inhibitor TH1020 (72 h). **e**,
803 Co-staining of TLR5 (red), SCGB3A2 (blue), and human nuclear antigen (HUNU,
804 white) in transplanted d-ALOs 4 weeks post-engraftment in NSG mice. Scale bars, 50
805 μm (low-magnification images), 20 μm (magnified images). Representative of two
806 independent transplants. **f**, Quantitative PCR analysis of inflammatory mediators in
807 PAO1 lysate-stimulated transplanted d-ALOs with or without 1 μM TH1020 (48 h). **g**,
808 Immunofluorescence of SCGB3A2 (green), CXCL8/CXCL10 (red), SFTPB/TLR5
809 (white), and DAPI (blue) in human lung sections from control and *Pseudomonas*
810 *aeruginosa*-infected COPD patients. White boxed area is expanded. Scale bars, 50 μm.
811 Representative of two patients per condition. **d**,**f**, Data are presented as mean
812 values ± s.e.m. *P*-values were calculated by one-way ANOVA and Tukey's multiple
813 comparison test. n=3 biological replicates.
814
815
816
817
818
819
820

821 **Extended Data figures**

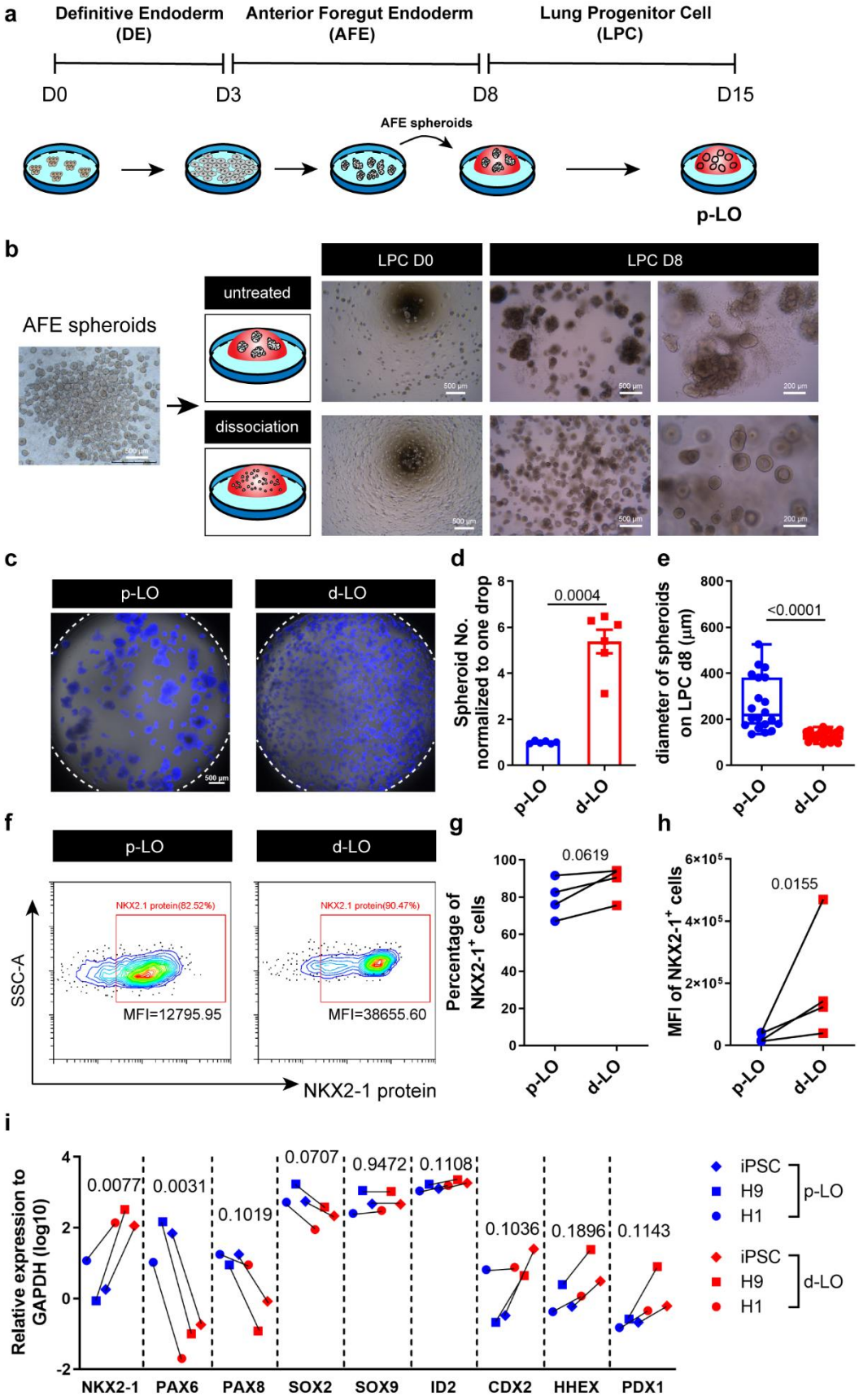

822

823 **Extended Data Fig. 1 Characterization of proximal and distal lung organoid**
824 **differentiation. a**, Differentiation protocol workflow for generating proximal lung
825 organoids (p-LOs) from hPSCs. **b**, Bright-field images comparing organoid
826 morphology under untreated versus dissociation conditions during lung progenitor cell
827 (LPC) induction. Scale bars, 500 μm (far left and middle two panels), 200 μm (right
828 panels). Representative of three biologically independent experiments. **c**, Phase-
829 contrast images of day 8 p-LOs and d-LOs counterstained with Hoechst. Scale bars,
830 500 μm. **d**, Organoid yield quantification (number per Matrigel droplet). **e**, Organoid
831 diameter measurements. **f**, Representative flow cytometry analysis of NKX2-1
832 expression in p-LOs versus d-LOs. n = 3 independent experiments. **g**,**h**, Percentage (**g**)
833 and mean fluorescence intensity (MFI) (**h**) of NKX2-1^{+} cells. **i**, qPCR analysis of lung-
834 specific and endodermal lineage markers in p-LOs and d-LOs derived from hESC lines
835 (H1, H9) and induced pluripotent stem cells (hiPSCs). **d**,**e**,**g**,**h**,**i**, Data are presented as
836 mean ± s.e.m. (n=3 biological replicates). *P*-values calculated using two-tailed
837 Student's *t*-test.
838
839
840
841
842
843
844

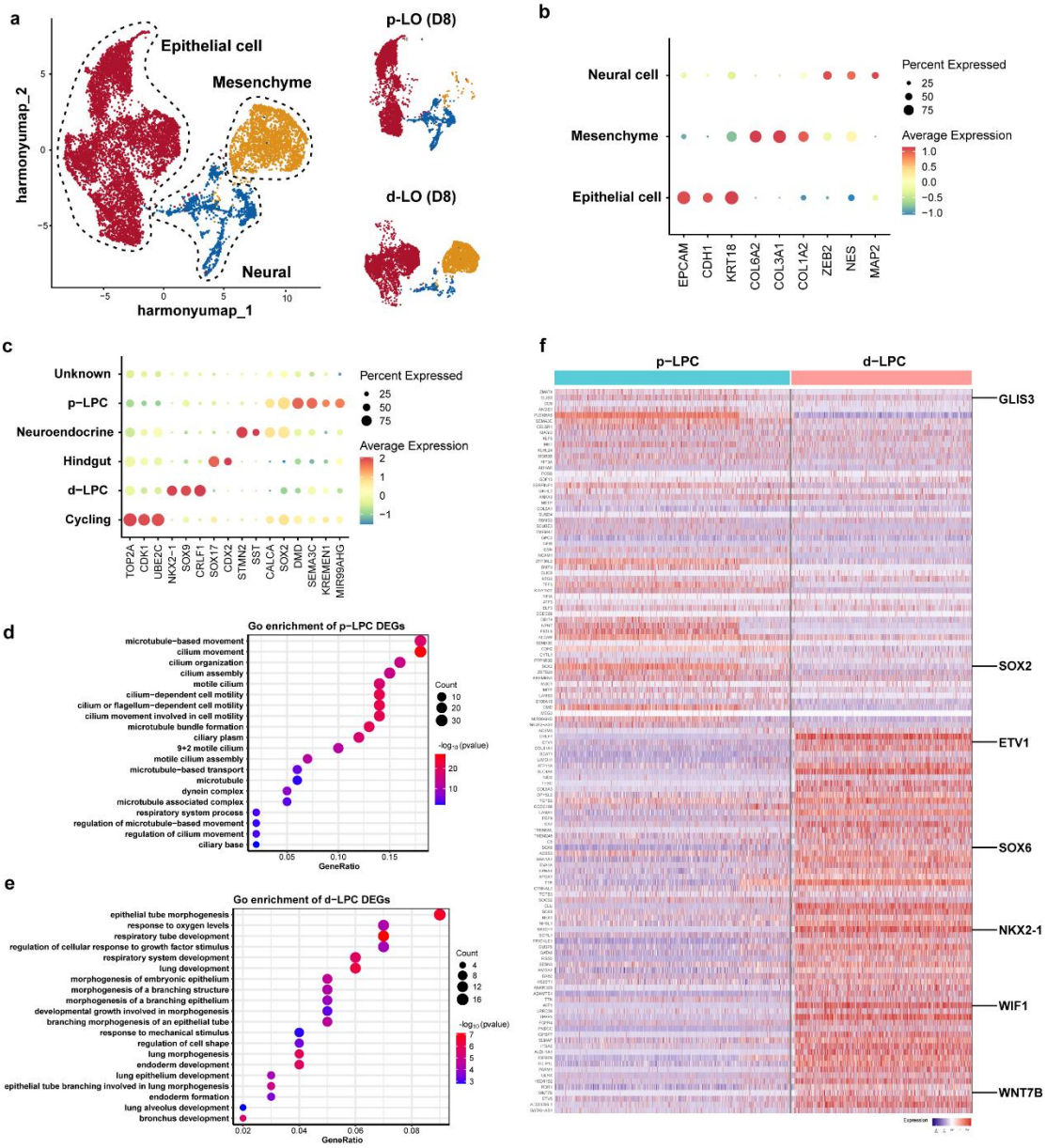

845

846 **Extended Data Fig. 2 Cellular characterization of lung organoids through single-**

847 **cell transcriptomics. a**, Integrated UMAP projection of p-LOs and d-LOs colored by

848 annotated major cell types (left) and experimental conditions (right). **b**, Dot plot

849 displaying canonical lineage markers for epithelial, mesenchymal, and neural cell

850 populations. **c**, Epithelial subcluster marker expression distinguishing d-LPC, p-LPC,

851 neuroendocrine cells, cycling cells, and hindgut-like cells. **d**,**e**, Gene Ontology (GO)

852 enrichment analysis of biological processes enriched in p-LPC (**d**) and d-LPC (**e**)

853 clusters. **f**, Expression patterns of proximal and distal lineage markers from fetal lung[15]

854 in p-LPC and d-LPC clusters.

855

856

857

858

859

860

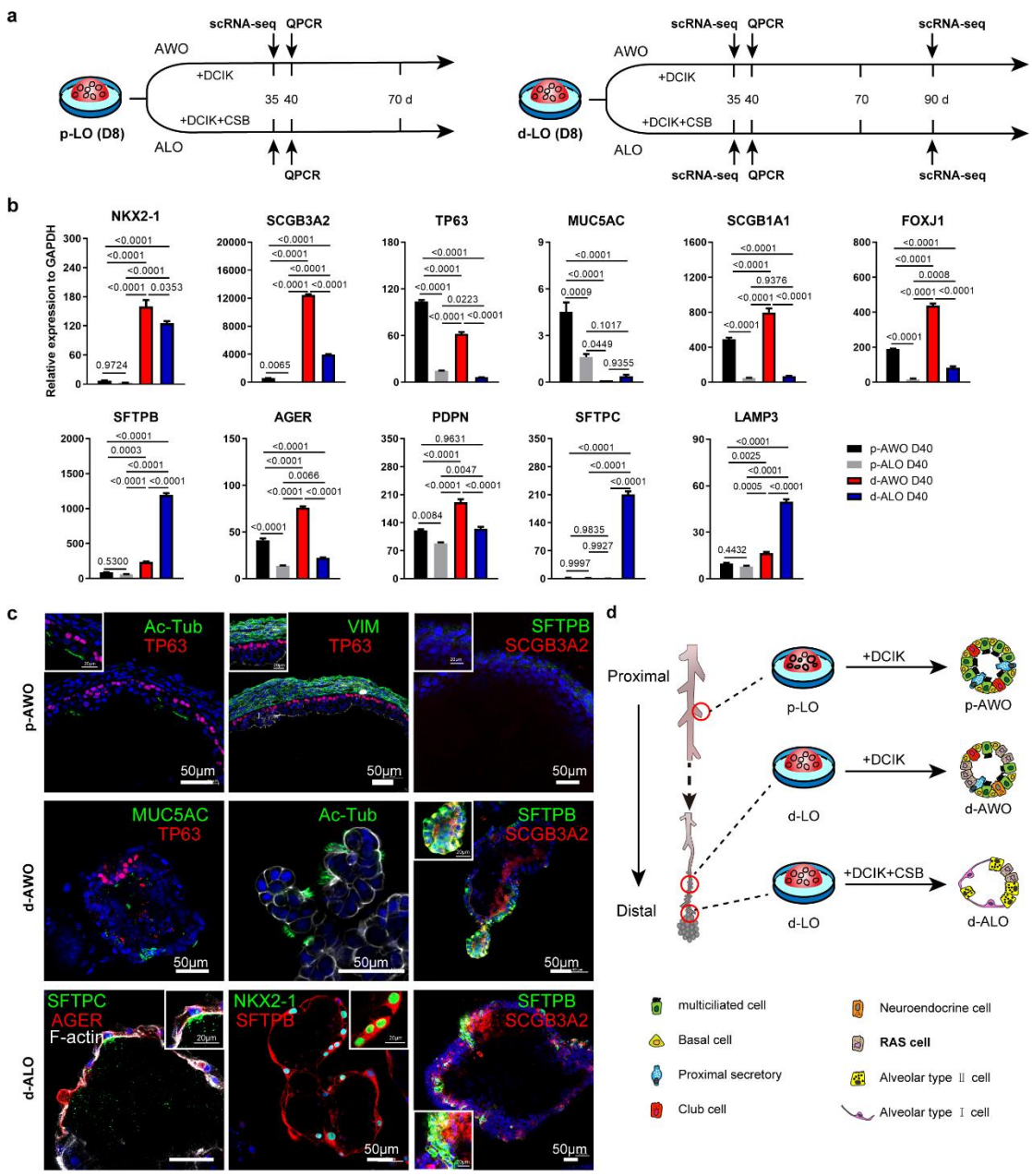

Extended Data Fig. 3 d-LOs generate distal airway and alveolar lineages containing RAS cells. a, Differentiation timeline for generating airway and alveolar organoids from proximal (p-LO) and distal (d-LO) lung organoids. Arrows indicate time points for qPCR and scRNA-seq analyses. **b**, qPCR quantification of lung lineage markers in p-LO- and d-LO-derived organoids. Lung epithelial marker: *NKX2-1*; Airway markers: *SCGB3A2*, *TP63*, *MUC5AC*, *SCGB1A1*, *FOXJ1*; alveolar markers: *SFTPB*, *AGER*, *PDPN*, *SFTPC*, *LAMP3*. Data are presented as mean ± s.e.m. (n=3).

869 *P*-values calculated by one-way ANOVA with Tukey's multiple comparison test. **c**,
870 Immunofluorescence co-staining of lineage markers in organoids: basal (TP63), distal
871 secretory (SCGB3A2, SFTPB), multiciliated (Ac-Tub), mesenchymal (VIM), goblet
872 (MUC5AC), AT2 (SFTPB, SFTPC, NKX2-1), and AT1 (AGER). Insets on select
873 images highlight protein expression in specific cells. Scale bars, 50 μm (low-
874 magnification images), 20 μm (expanded insets). Representative of three independent
875 experiments. **d**, Schematic of regional lineage specification from proximal airway and
876 distal airway/alveolar organoids.
877
878
879
880
881
882
883

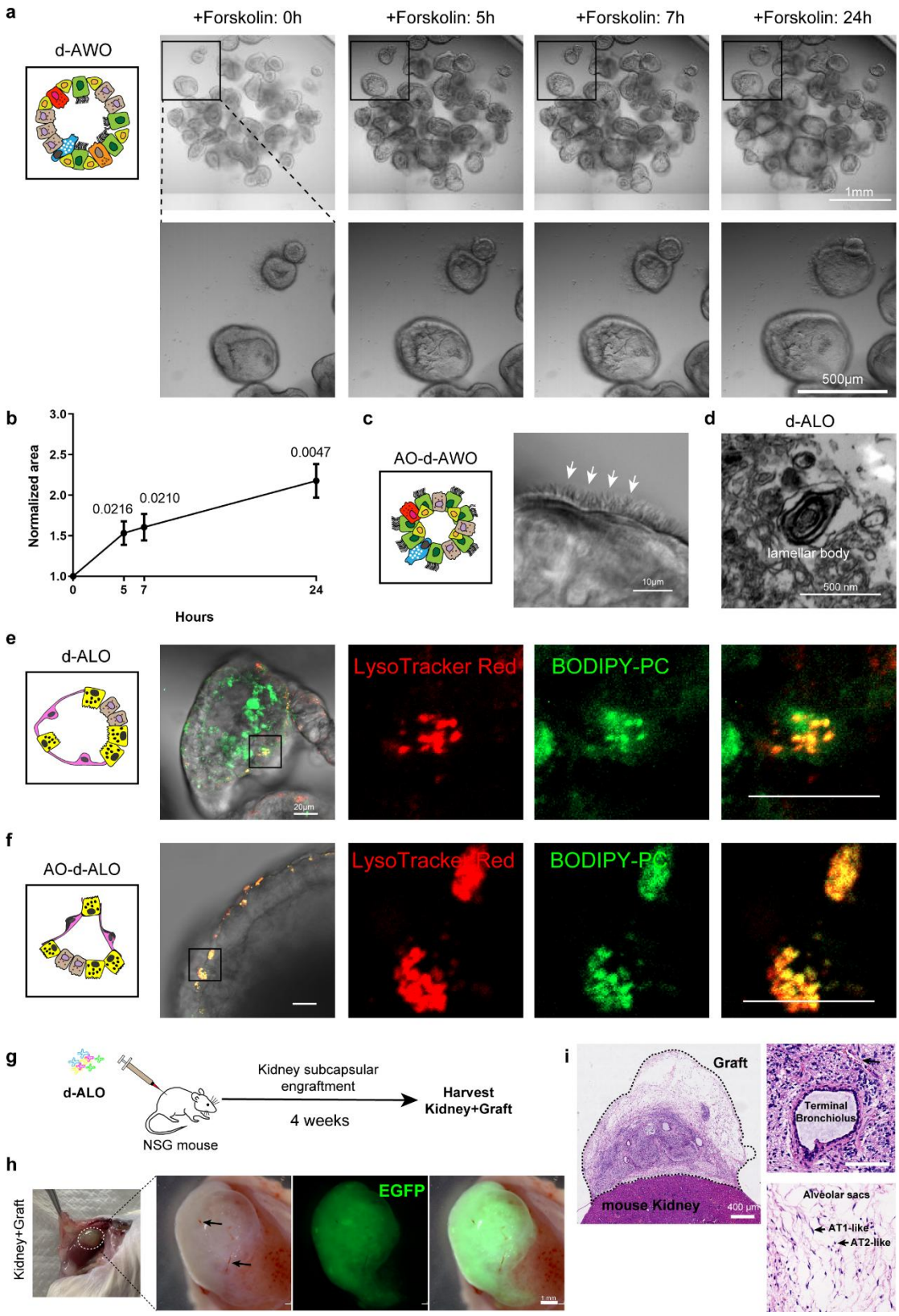

884

885 **Extended Data Fig. 4 Functional validation of distal lung organoid derivatives. a,**

886 Time-lapse phase-contrast imaging of forskolin-induced swelling in distal airway

887 organoids (d-AWO) derived from d-LOs. Scale bars, 1 mm (upper panel), 500 μm
888 (lower panel). **b**, Quantification of normalized luminal swelling area in d-AWOs over
889 24 hours. Bars represent mean ± s.e.m. (n=20 organoids). *P*-values calculated using
890 two-tailed Student's *t*-test. **c**, Schematic of apical-out (AO) polarity model (left) and
891 representative microscopy showing cilia in AO-d-AWO. Scale bar, 10 μm. **d**,
892 Transmission electron microscopy (TEM) of d-ALOs showing lamellar body-like
893 structures. Scale bar, 500 nm. **e**,**f**, BODIPY-labeled phosphatidylcholine uptake in
894 Matrigel-embedded (**e**) and apical-out (**f**) d-ALOs. Scale bars, 20 μm. Representative
895 of three independent experiments. **g**, Workflow for subrenal capsule transplantation of
896 d-ALOs into NSG mice. **h**, Macroscopic images of transplanted d-ALOs (green) at 4
897 weeks post-engraftment. Arrows indicate vasculature. Scale bar, 1 mm. **i**, Hematoxylin
898 and eosin (H&E) staining of d-ALO grafts at 4 weeks post-transplantation. Scale bar,
899 400 μm.
900

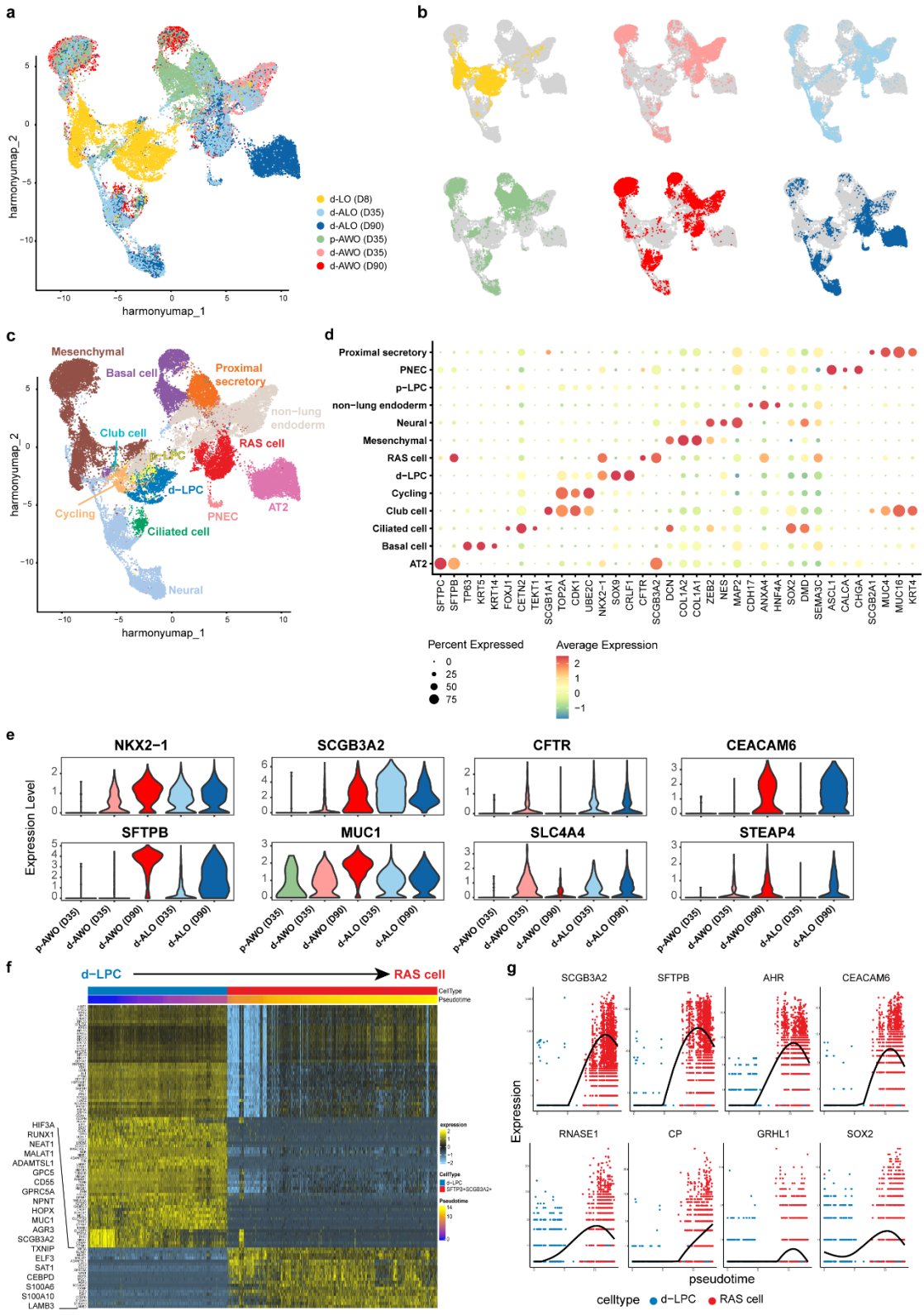

Extended Data Fig. 5 Characterization of cell populations in differentiating lung organoids from proximal and distal lineages using single-cell RNA sequencing. a,**b**, UMAP projections of single-cell RNA sequencing data from d-LOs and organoids

905 under differentiation conditions, colored by all (**a**) or individual differentiation
906 time/media conditions (**b**). **c**, Annotated UMAP distinguishing major cell types across
907 differentiation conditions. **d**, Dot plot of canonical markers defining cell clusters in (**c**).
908 **e**, Violin plots illustrating the expression of *NKX2-1*, *SCGB3A2*, *CFTR*, *CEACAM6*,
909 *SFTPB*, *MUC1*, *SLC4A4*, and *STEAP4* within the RAS cell cluster across different
910 time/media conditions. **f**, Heatmap of gene expression dynamics along the
911 pseudotemporal trajectory from d-LPCs to RAS cells (pseudotime scale above). **g**,
912 Smoothed expression patterns of select lineage-associated genes during d-LPC-to-RAS
913 cell differentiation.

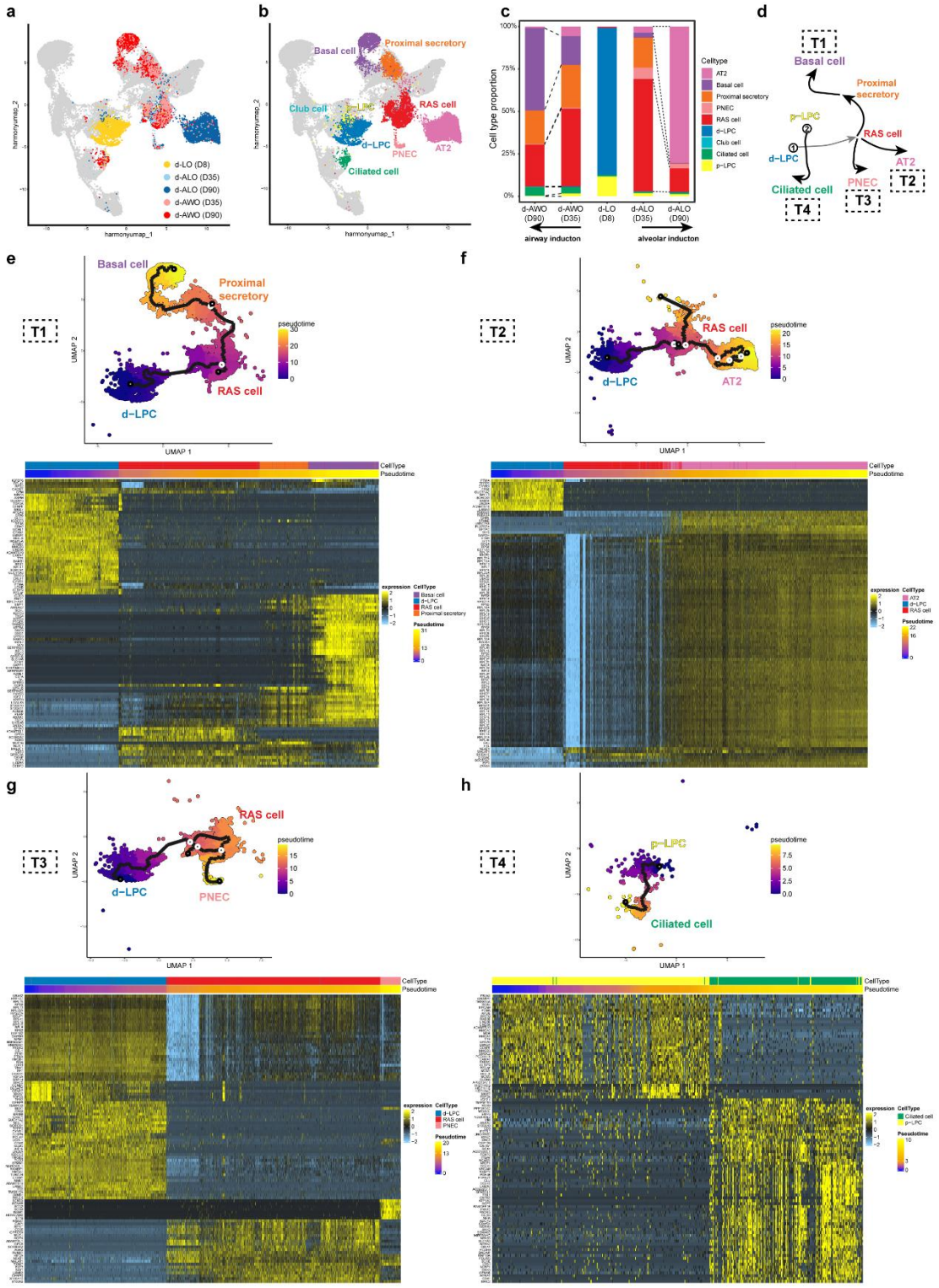

914

915 **Extended Data Fig. 6 Lineage potential of RAS cells in d-LO-derived organoids.**

916 **a**,**b**, UMAP projections of single-cell transcriptomes from d-LOs and their derivatives.

917 Cells colored by experimental conditions (**a**) or annotated cell types (**b**). **c**, Proportional

918 distribution of cell types in d-LOs versus d-LO-derived organoids. **d**, Schematic

919 showing trajectory analysis identifying four differentiation paths from RAS cells to
920 PNEC, basal, and AT2 lineages as well as from p-LPC to ciliated cell. **e-h**, UMAP
921 projections depicting four cellular trajectories with color indicating progression (top)
922 and heatmaps of trajectory-defining gene expression (bottom) across pseudotime for
923 each lineage relationship.
924
925
926
927
928
929

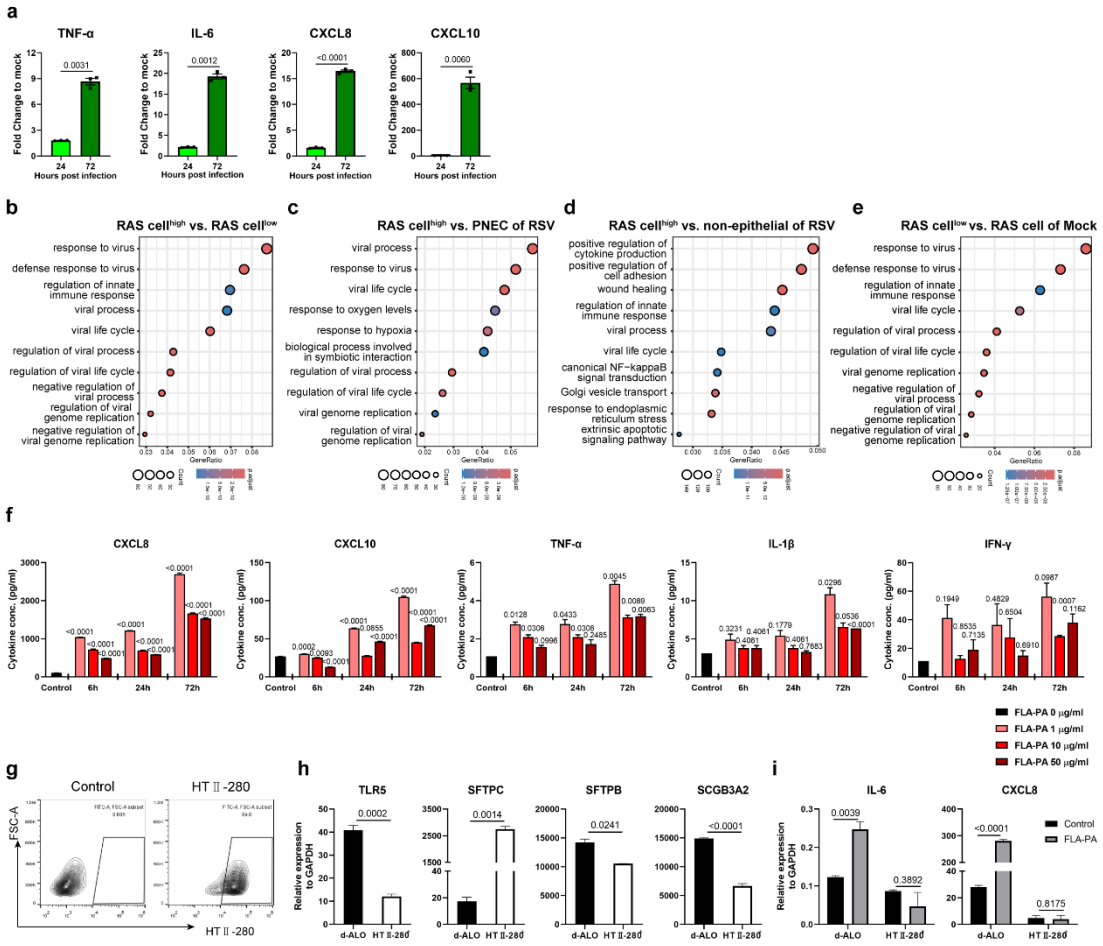

Extended Data Fig. 7 Immune defense capacity of RAS cells in d-LO derived organoids. a, qPCR analysis of *CXCL8*, *CXCL10*, *IL-6*, and *TNF-α* expression in d-ALOs infected with RSV (MOI 0.1) at 24 and72 hours post-infection (hpi). **b-e**, GO enrichment analysis of RAS cell^{high} versus the other clusters in infected organoids and RAS cell^{low} versus mock. **f**, Cytokine/chemokine secretion (CXCL8, CXCL10, IL-6, IL-1β, TNF-α) from d-ALOs stimulated with increasing concentrations of FLA-PA protein (1–50 μg/ml) over 6–72 hours. Data are presented as mean ± s.e.m. (n=3 biological replicates). **g**, Flow cytometry gating strategy for AT2 cell isolation using HTII-280 surface marker. **h**, qPCR validation of *TLR5*, *SFTPC*, *SFTPB*, and *SCGB3A2* expression in sorted HTII-280^{+} AT2 cells, confirming high alveolar (*SFTPC*) and low immune (*TLR5*) signatures. **i**, Comparative RT-PCR analysis of *CXCL8* and *IL-6* in

942 whole d-ALOs versus sorted HTII-280^{+} AT2-enriched organoids after 72 h FLA-PA

943 stimulation (1 μg/ml). **a**,**f**,**h**,**i**, Data are presented as mean ± s.e.m. (n=3). *P*-values

944 calculated using two-way ANOVA (**f**) or two-tailed Student's *t*-test (**a**,**h**,**i**).

945

946